PHOTOCATALYTIC HYDROGEN PRODUCTION USING METALLIC SILVER LOADED CALCIUM TITANATE PHOTOCATALYST

By AZZAH ALZAHRANI

A thesis submitted to the

Graduate School-Camden

Rutgers, The State University of New Jersey

in partial fulfillment of the requirements

for the degree of Master of Science

Graduate Program in Chemistry

written under the direction of

Dr. Alexander Samokhvalov

and

approved by

_____

Alexander Samokhvalov

_____

Alex J. Roche

_____

George Kumi

Camden, New Jersey

May 2016

THESIS ABSTRACT

Photocatalytic Hydrogen Production Using Metallic Silver Loaded Calcium Titanate Photocatalyst

By AZZAH ALZAHRANI

Thesis Director:

Dr. Alexander Samokhvalov

Photocatalytic hydrogen production by water splitting has been widely studied as one of the promising solutions for energy and environment problems. Perovskite alkaline earth metal titanates are capable of splitting water and producing hydrogen due to their electrical, optical, catalytic properties. Calcium titanate is one of the promising semiconductors because of its wide band gap and its high stability against photo-corrosion in acidic and wet environments.

This research focuses on the investigation of the photocatalytic activity for hydrogen generation using metallic silver loaded on calcium titanate in the presence of a sacrificial electronic donor, glycerol, and under UV and visible light. Nanocrystalline $CaTiO_3$ showed photocatalytic activity under UV light due to charge transfer from the semiconductor to the metal, and this process was proved using photoluminescence spectroscopy. The characterizations of nanocrystalline calcium titanate were conducted using Raman, UV-vis diffuse reflectance, and photoluminescence spectroscopy.

In this research, we have also investigated the capability of metallic silver deposited on mesoporous calcium titanate to decompose water and produce hydrogen under UV light without a sacrificial organic donor. Further, by using emission and synchronous

photoluminescence spectroscopy, we studied the midgap states within the forbidden gap in the semiconductor, and the effect of humidification on these midgap states.

Dedication

This thesis is dedicated to my family, my husband Tariq, little children Eliana and Mohammed, and my mother Maryam. The encouragement and support that they gave me throughout my study assisted me to complete my degree.

Acknowledgements

I would like to express my gratitude and appreciation to Dr. Alexander Samokhvalov, who was my M.S. thesis advisor, for ideas and support through this research. Thank you for helping me to develop my research skills and for truly enriching my learning experience. I would also like to thank my M.S. committee members: Dr. Alex J. Roche and Dr. George Kumi for their help with reviewing my thesis and their advice on my research. I thank the faculty, staff members, and graduate students in Chemistry Department whom I had the pleasure to work with during my graduate studies at Rutgers University.

Table of Contents

List of Figures

List of Tables

1. Introduction

The need for clean energy is one of the most significant requirements for the future of human society. In order to solve the problems associated with the depletion of fossil fuels and the burning of natural gas on the environment (which contributes to greenhouse gasses, such as carbon dioxide and methane), a new renewable energy resource must be developed [1]. Hydrogen produced from water by solar energy is considered an alternative resource that is low-cost and environmentally friendly. Many studies have been reported for hydrogen production using photoelectrochemical water splitting over tantalates, niobates, and titanate-based materials [2, 3]. Further, other oxide semiconductors, such as perovskite alkaline earth metal titanates, can be utilized for hydrogen production [4, 5].

1.1. Perovskite alkaline earth metal titanates

Among the majority of metal oxide photocatalysts, perovskite-based oxides have particular photochemical properties and offer distinct advantages [4]. Perovskites have the general formula ABO_3. Generally, in this crystal structure, A presents larger cation (e.g. Mg, Ca, Sr, etc.), and B is the smaller cation such as Ti [4]. Many perovskite ABO_3 compounds have a simple cubic structure with O atoms at the face centers coordinated to metal atoms B in the body center and A at the cube corner, Figure 1.1.

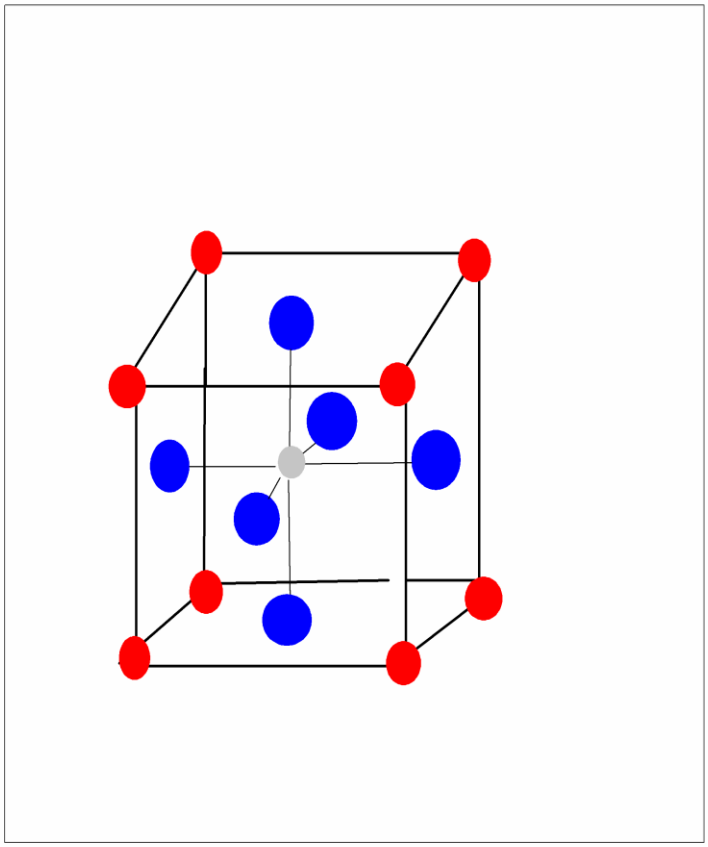

Figure 1.1. Structure of cubic perovskite

$CaTiO_3$ is one of the alkaline earth titanates which is thermally and chemically stable and has three different crystal structures: cubic, orthorhombic, and tetragonal [6, 7, 8]. Each lattice structure has a number of defects that allow a broad range of potential technological applications [7]. Among these structures, the orthorhombic lattice structure is complex due to the large uncertainty of its structural parameters [9]. From Figure 1.2, it can be observed that orthorhombic $CaTiO_3$ has two different oxygen sites, O_1 and O_2. The Ca is coordinated by O atoms. Ti atom is the center of the octahedron formed by oxygen atoms [9].

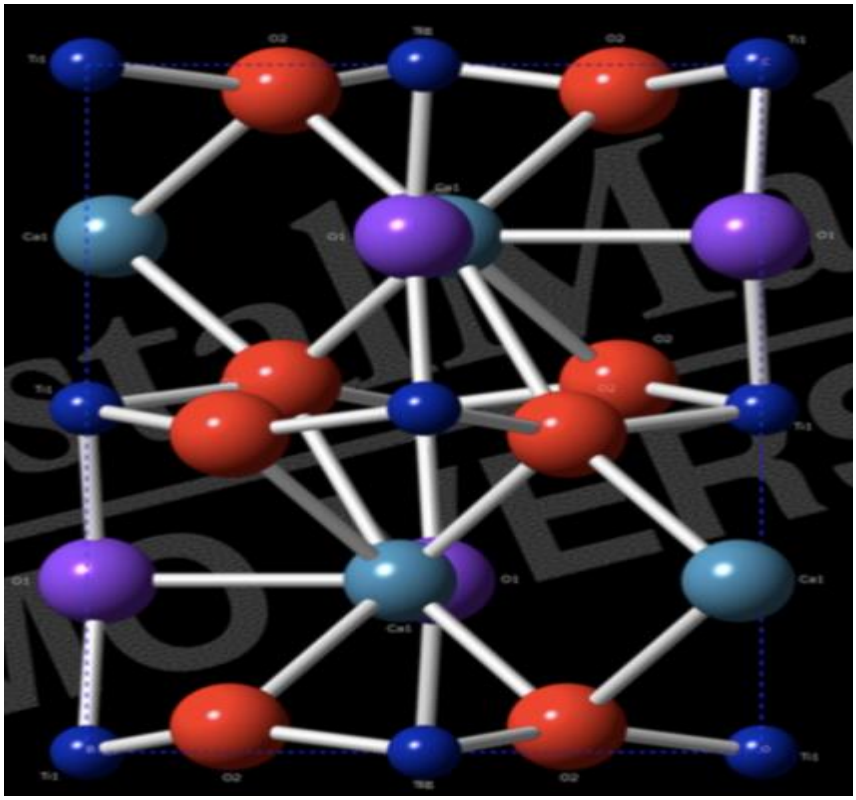

Figure 1.2. The crystal structure of orthorhombic $CaTiO_3$

Different degrees of tilting of the octahedron cause different crystal fields which result in varying electronic properties. For example, rotation of TiO_6 octahedra in the case of $CaTiO_3$ results in distortions [8]. Thus, the level of tilting might influence the band gap, electron/hole separation, and photoluminescence [4].

1.2. Mesoporous calcium titanate

Porosity is defined as the presence of holes or channels in the lattice which increase the ability of the materials to interact with other ions or atoms [10]. According to the International Union of Pure and Applied Chemistry (IUPAC) [11] mesoporous materials contain pores between 2 nm-50 nm. Materials that have pores > 50 nm are called macro-porous while materials with pores < 2 nm are microporous. Generally, the interaction of

porous materials could be on the surface or throughout the bulk [12]. Further, these pores could be opened or closed depending on the ability to adsorb other molecules [10].

Mesoporous calcium titanate has unique physical and chemical properties such as pore structure and high surface area [13]. Moreover, mesoporous calcium titanate could exhibit particular properties such as size selective absorption and coupled electronic properties [12]. Therefore, the porosity of $CaTiO_3$ can enhance its application in areas of photocatalysis [14], electronics [10], gas separation [12], and sensors [12].

1.3. Structural characterization of mesoporous semiconductors

Gas adsorption plays an important role in the characterization of a wide range of porous materials [10]. Even though there are many gases that can be used as an adsorbent, such as argon, carbon monoxide, carbon dioxide, and krypton, nitrogen gas is the most common adsorbent (an average molecular area of ~ 0.162 nm^2) [15]. An adsorption isotherm measures the amount of gas adsorbed across a range of relative pressures at constant temperature (77 K), Figure S.1 (supplementary). Conversely, a desorption isotherm is achieved by measuring gas removed as pressure is reduced [15].

Figure S.1. [10] The types of the adsorption isotherm

The use of nitrogen adsorption requires a degassing process that is an important step before the measurement of surface area or pore size. The surface can be cleaned from water and organic vapors by heating under vacuum or flowing of dry air. The goal of degassing is to achieve maximum adsorption capacity and to avoid any modification as a result of the surface change [15].

1.3.1. Brunauer–Emmett–Teller (BET) method

The BET method is the most common way to determine the surface area of catalysts and other materials. The BET theory is based on the idea of molecular adsorption [16]. In this theory, the adsorbent surface works as equivalent sites to adsorb other molecules in a random manner [15]. It is hypothesized that there are no interactions between the adsorbed molecules which make the first monolayer and act as sites for molecules in the second layer. It is also assumed that the higher layers of adsorbed molecules have liquid-like properties [10]. For instance, the structure of the nitrogen monolayer is dependent on the surface chemistry of the adsorbent since the nitrogen molecule is quadrupolar. However, the multilayer structure is rather insensitive to the nature of the adsorbent. In general, the BET monolayer capacity should be obtained from the best linear fit of the isotherm [15].

1.3.2. Barrett, Joyner, and Halenda (BJH) method

BJH is the most popular method to determine the pore size distribution of the semiconductors [12]. It is based on the hypothesis of the cylindrical shape of the pores, and the modified Kelvin equation. The BJH method relates the amount of adsorbate removed from the pores of the mesoporous solid to the size of the pores as the pressure (p/p^0) is reduced from high to low value [10].

1.4. Spectroscopic characterization of semiconductors

1.4.1. Raman spectroscopy

Raman spectroscopy is a useful tool to detect small shifts in the frequencies of normal modes that result from small differences in parameters of crystal structure like bond lengths or bond angles [17]. Further, vibrational Raman spectroscopy can provide valuable information for understanding the behavior of nanoscale semiconductors [18]. This accuracy makes this experimental technique a very efficient tool for structural study. An example of a Raman spectroscopy application is to study changes in a semiconductor structure and distinguish between different crystal structure.

1.4.2. UV-vis diffuse reflectance spectroscopy (DRS)

The separation between the minimum energy of the conduction band and the maximum energy of the valence band is called the band-gap or forbidden energy gap (E_g), and it is one of the most important properties of a semiconductor. Moreover, the properties of the semiconductors are mainly affected by the E_g parameters [20]. Electrons in a solid occupy allowed energy bands, and the band gap energy (E_g) can be evaluated by plotting the highest valence band edge and the lowest conduction band edge [21].

In general, there are two types of band-to-band transitions:

1. Direct transitions or direct gaps which could be allowed when the material has strong light absorption and a phonon with enough energy (E) is not required to conserve the momentum [22] which means the change of electron momentum is zero. Direct transitions also can be forbidden [23].

2. Indirect transitions, when at least one phonon carries little momentum and participates in the absorption or emission of light [22]. In other words, the change of electron momentum is non-zero [23]. It is obvious that indirect and direct transitions can occur in all semiconductor material.

Through many years, several methods have been developed and applied to evaluate E_g from the optical absorption spectra and diffuse reflectance spectra as well. Among these characterization techniques, UV-vis diffuse reflectance spectroscopy is one of the most applied methods due to its ability to describe the electronic behavior present in the structure of the solid [22]. The optical methods used for measuring forbidden energy band gaps do not depend on temperature variations or uncertainties due to surface states. However, a given semiconductor may have different values of E_g depending on the calculation method (e.g. Kubelka–Munk method, Tauc plot, etc..) and electronic transition (allowed or forbidden and direct or indirect transition) [23].

In principle, band gap determination using UV-vis diffuse reflectance spectroscopy depends on the excitation of the electrons from the valence band to the conduction band which is observed by an increase in the absorbance at a given wavelength (band gap energy). In the literature, the band gap can be obtained from the Kubelka–Munk theory t which may have several modifications depending on the specific application and limitation. Generally, the original Kubelka–Munk theory should be used where its accuracy is sufficient, as in photocatalysis [24].

The band gap of semiconductor particles can be obtained by plotting the following expression proposed by Tauc, Davis, and Mott [24]:

$$(h\nu\alpha)^{1/n} = A\,(h\nu - Eg) \qquad (1)$$

where h is Planck's constant, ν is a frequency of vibration, and α is the absorption coefficient. Eg is band gap, and A is a proportional constant in the equation. Usually, n = 1/2 for a direct allowed transition, and n = 2 for an indirect allowed transition. After that, the acquired diffuse reflectance spectrum is converted to the Kubelka-Munk function in which α in the Tauc equation is substituted with F(R∞) [20] which is proportional to the absorption coefficient. Therefore, the expression becomes:

$$(F(R)\ h\nu)^{1/n} = A\ (h\nu - Eg) \qquad (2)$$

1.5. Semiconductor photocatalysis

Heterogeneous photocatalysts that can capture a photon and use the photon for water photolysis are typically semiconductors, which are well-defined by the band gap energy. The band gap is the minimum energy required to promote electrons from the valence band to the conduction band. This phenomenon can be used to split water to produce H_2 and O_2 [2]. Photolysis of water can be achieved by absorbing light with a wavelength between 190 nm - 800 nm (UV-visible region). In this process, photons that have energy equal or greater than the band gap are absorbed by the semiconductor. An electron is excited from the valence band to the conduction band leaving an empty state called a hole in the valence band, Figure 1.3. The recombination of the hole with water results in two half reactions [25]:

$$H_2O + 2h^+ \rightarrow 2\ H^+ + 1/2\ O_2 \text{ (oxygen evolution)} \qquad (3)$$

$$2\ H^+ + 2\ e^- \rightarrow H_2 \text{ (hydrogen evolution)} \qquad (4)$$

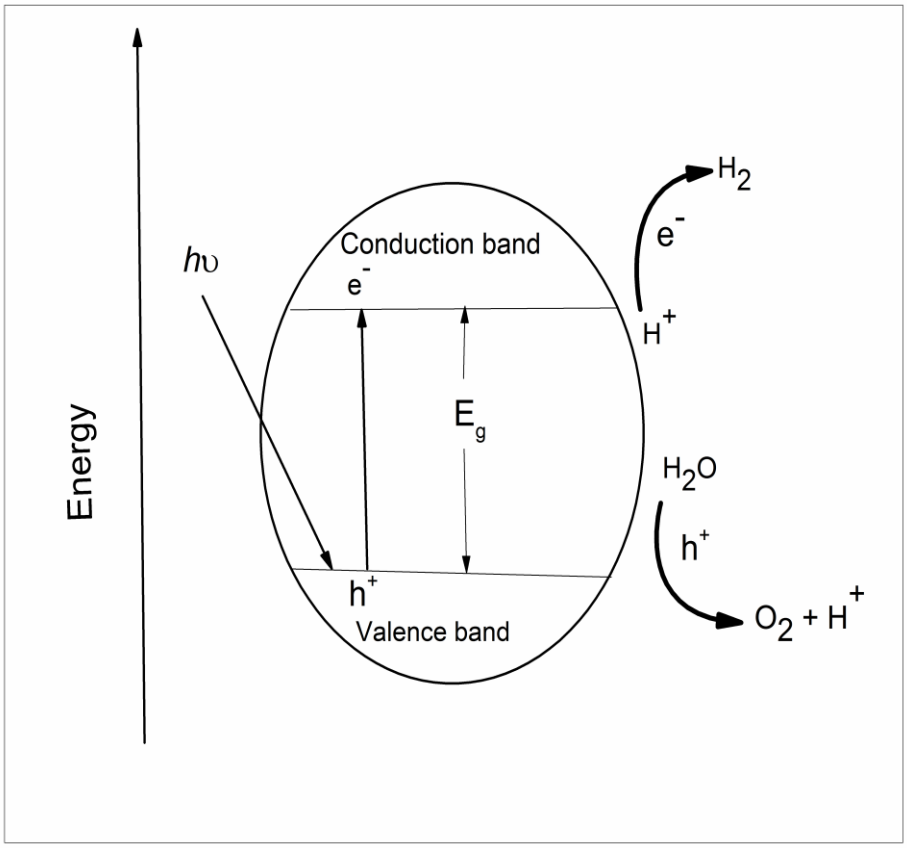

Figure 1.3. Semiconductor photocatalysis process

Hence, the semiconductor should have a potential of the top of valence band more positive than 1.23 eV (oxygen evolution half- reaction potential) vs. normal hydrogen electrode (NHE), to be able to produce oxygen. Further, the potential of the conduction band minimum should be more negative than zero (hydrogen evolution half-reaction potential) vs. NHE [26] to generate hydrogen.

Amongst oxide semiconductor photocatalysts, titanium dioxide has proven [25] to be a suitable candidate for photocatalytic water splitting due to its photo- and chemical properties, strong oxidizing ability, and high chemical stability against corrosion [27]. However, the hydrogen production efficiency by photocatalytic water splitting on TiO_2 is

still very low, basically because of the following reasons: (1) the recombination of photogenerated conduction band (CB) electrons and valence band (VB) holes on the surface of TiO_2 which results in fast reverse reaction between hydrogen and oxygen [2], and (2) at about - 0.3 eV with respect to NHE, the conduction band minimum (CBM) of TiO_2 is only slightly more negative in potential than the hydrogen evolution half-reaction potential (the valence band minimum (VBM) is positive enough for water oxidation) [28].

The more negative the potential of the CBM, the greater the ability of a semiconductor to produce hydrogen. Thus, alkaline earth metal titanates, with their more negative CBM potentials [26] (relative to titanium dioxide) are more attractive photocatalysts for hydrogen generation. Amongst alkaline earth metal titanates, calcium titanate $CaTiO_3$ has the most negative CBM potential (Figure 1.4), and it has been studied as a photocatalyst for hydrogen generation [29].

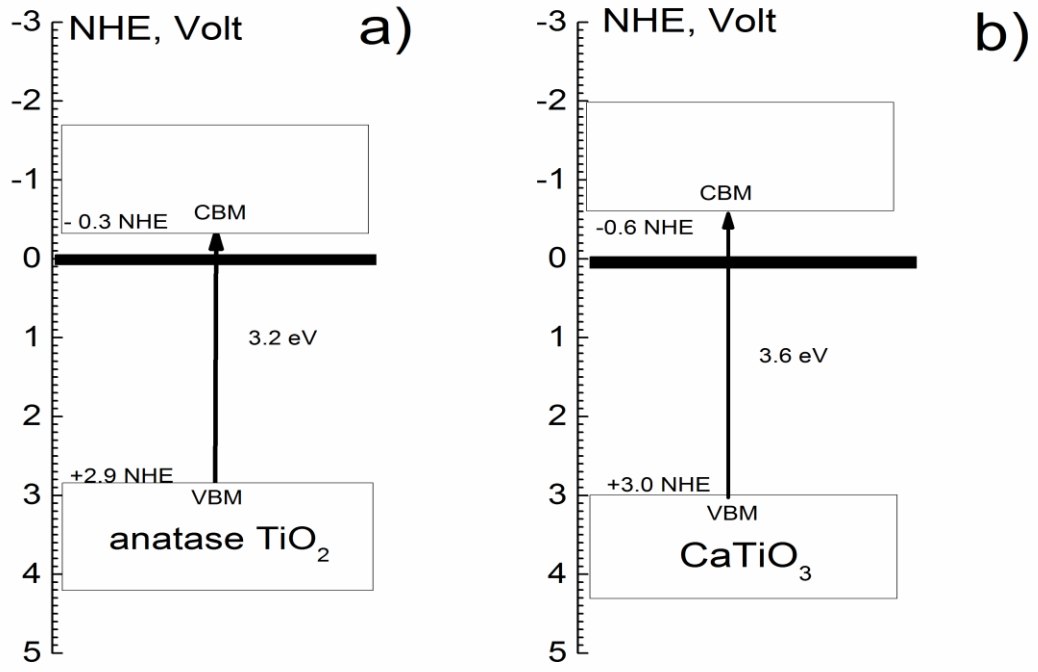

Figure 1.4. Scheme presenting the positions of the valence band and the conduction band edges vs. NHE for a) TiO_2 and b) $CaTiO_3$.

However, the recombination and separation/migration processes [4] are the two important competitive processes for the photoexcited electron, and they affect the stability of the photocatalysts. Therefore, the photocatalysis efficiency for most semiconductor photocatalysts is too small to be applied in the industry. The main cause of this low efficiency is the photogenerated electron-hole recombination in the bulk or at the surface of the photoexcited particles [5].

1.6. Recent progress

1.6.1. Metal-$CaTiO_3$ for hydrogen generation with sacrificial donor

Calcium titanate is one of the perovskite minerals, and its reported [29, 30] bandgap is in the range 3.4 - 3.9 eV or within 318 - 365 nm. It has been reported that calcium titanate has the ability to split water and generate hydrogen under UV light irradiation with a sacrificial donor. However, $CaTiO_3$ cannot produce hydrogen under visible light irradiation unless metals such as Cu, Pt [31], and Ag-La [32] are doped into the semiconductor. Also, the presence of sacrificial organic donors is needed as can be seen from Table 1. Metals may not only promote visible light absorption but also increase hydrogen production under UV radiation.

Table 1: Photocatalytic hydrogen production of doped $CaTiO_3$ with a donor.

Donor	Donor Volume, ml	Mass of catalyst, g	V reactor, ml	Metal promoter	Amount of promoter, wt%	Photo-excitation light, λ	H_2 Rate, μmol/h	Rate, recalc. μmol/g.h	Ref.
methanol	20	1	420	Cu	0.02	> 400 (350 W high-pressure Hg lamp	1447	1447	[3]
methanol	60	0.5	540	Rh	0.05	400 W-Hg lamp	900	1800	[30]
methanol	20	0.1	100	Pt	0.1	= 320-390 nm by 300 W Xe lamp	260	2600	[31]
methanol	30	0.1	100	Fe	0.05	= 420 nm via UV or Visible light arc-discharge bulb.	131	1310	[29]
methanol	20	0.1	420	Ag-La	0.03	> 400 (350 W high-pressure Hg lamp	106	1060	[32]

1.6.2. Metal-$CaTiO_3$ for H_2 production without donor

When different amount of metals, such as Pt, Ru, Ni, and Ir, were doped on $CaTiO_3$ without a sacrificial donor, an evolution of H_2 and O_2 was observed with Pt and Ru. For instance, it was found that 0.1 wt.% of Pt impregnated on 0.5 g $CaTiO_3$ exhibited the highest evolution rate, 38 µmol/h (76 µmol/g.h) of H_2 gas and 19 µmol/h O_2 gas while doping the same amount of the Ru, Ni, and Ir showed 10 µmol/h, 5 µmol/h, and 8 µmol/h of H_2 rate respectively. Therefore, Pt is the most efficient co-catalyst that could promote hydrogen production without a sacrificial donor [33].

1.7. In-situ photocatalysis

In situ photo-assisted deposition of a co-catalyst onto a semiconductor is an alternative method to the doping technique [12]. Photo-assisted deposition has many advantages [34]: (1) It is a simple and convenient method that does not affect the crystal structure of the photocatalyst. (2) It results in the homogeneous dispersion of the co-catalyst on the surface of the semiconductor which creates great interfacial contact between them. (3) It leads to the direct formation of co-catalyst in a short time with effective carrier charge separation.

1.8. Sacrificial electron donor (SED)

The addition of sacrificial reagents (electron donors) into a photocatalytic reaction has been investigated for photocatalytic hydrogen production [5]. Many organic compounds in wastewater such as amines and alcohols are efficient electron donors and can be used as sacrificial donors for photocatalytic hydrogen generation [28]. The SED provides electrons and hydrogen for the reductive half-reaction of the photocatalysis. For this reason, it has been proven that this process improves the efficiency of photocatalytic hydrogen production rates [5]. However, if the sacrificial electron donors are fuels, such as methanol

or ethanol, or its cost is much higher than that of hydrogen production, their use for hydrogen production is worthless. In contrast, the use of organic wastes or industrial pollutants as sacrificial reagents, followed by their conversion into environmental friendly products is highly beneficial [35]. For instance, glycerol is an industrial byproduct that produces from biodiesel economics. Glycerol is also a common industrial waste originating from some chemical processes [27]. Therefore, there is a need to transfer the glycerol into an environmentally friendly product as a sacrificial reagent that is effective in photocatalytic water splitting.

1.9. Silver nanoparticles (Ag NPs)

Nobel metal nanoparticles have attracted research due to their optical, electrical, and catalytic properties [36]. By controlling their shape, size, and chemical composition, metal nanoparticles can be used widely in different applications; for example, a co-catalyst with semiconductors [37], antibacterial [38], and electronic materials.

As mentioned before, alkaline earth semiconductors have a large band gap, so most of them are only active under UV light. Thus, many attempts have been made to develop photocatalysts that have the ability to absorb visible light. It is well known that noble metals including gold, copper, and silver nanoparticles absorb visible light because of the Surface Plasmon Resonance (SPR) effect [37]. Further, silver nanoparticles (Ag NPs) exhibit UV light absorption due to the interband transition. Thus, Ag NPs can utilize the full solar spectrum [36].

1.10. Photoluminescence (PL) spectroscopy

Photoluminescence is known as the spontaneous radiative emission of a photon due to an electron that is (1) photo-excited to a higher energy state (e.g. the conduction band) by

absorbing appropriate energy and (2) then makes a transition to the lower energy state (e.g. valence band) [16]. The energy that is applied as external light has to be greater than or equal to the energy of the band gap of the semiconductor [39], $h\nu \geq E_g$.

1.10.1. Excitation and emission PL spectra

In conventional photoluminescence spectroscopy, two types of spectra are measured: excitation and emission spectra. When a sample is excited at a fixed wavelength λexc, an emission spectrum is produced by measuring the emission intensity as a function of the emission wavelength λem. An excitation spectrum may be obtained when λexc is scanned while the observation is conducted at the fixed λem [16].

The absorption of light occurs very quickly and corresponds to excitation of the electron from the ground state to an excited state [16]. The emission of a photon through fluorescence or phosphorescence is also measured in quanta. The energy is expressed by the equation:

$$E = h\nu = hc/\lambda \qquad (5)$$

where E is the energy, h is Planck's constant, ν is the frequency, c is the speed of light, and λ is wavelength of the photon. Planck's law indicates that the radiation energy of a photon is directly proportional to the frequency and inversely proportional to the wavelength. On the other hand, the shorter incident wavelengths correspond to a greater quantum of energy [16].

Photoluminescence emission spectra at different excitation wavelengths have their own characterization. The emission spectrum is usually independent on the excitation wavelength as a result of the rapid internal relaxation to the lowest vibrational energy level

of the excited state. In many materials, the detailed vibrational structure is lost, and the emission spectrum appears as a broad band [39].

1.10.2. Synchronous PL spectroscopy

Even though in conventional photoluminescence, one can select the excitation and the emission wavelength, conventional photoluminescence has a limited capability of spectral resolution [40] capability, and often overlapped spectra are obtained [41]. Another technique with a high selectivity can be used to provide high-resolution spectra and narrow bands; this technique is called synchronous luminescence spectroscopy [41]. In synchronous luminescence, it is possible to vary the emission and excitation wavelength while keeping a constant difference $\Delta\lambda$, and when the optimum $\Delta\lambda$ is obtained, the spectrum consists of narrow and distinct spectral bands [40].

1.10.3. The effect of variable temperature on PL spectra

At room temperature, most electrons occupy the lowest vibrational level of the ground electronic state, and when they absorb an appropriate amount of light, they are elevated to the excited states [42]. Excitation can result in an electron reaching any of the vibrational levels associated with each electronic state. Since the materials absorb the energy as quanta [43], this could result in a series of absorption bands which may not be fully resolved due to the neglected rotational levels from the transition [44, 45]. However, at cryo temperatures (77 K), the spectral widths are usually reduced, and the spectra exhibit enhanced vibrational information [44].

Photoluminescence is one of the useful tools to study the characterization of materials, and it can provide detailed information about recombination processes between electrons and holes, defect levels, surface and interface impurities, and band gap.

1.10.4. Free carrier recombination (band to band transition)

Free carrier recombination requires the presence of an electron in the conduction band and a hole in the valence band of the semiconductor. It occurs when the excitation energy is greater than or equal to the band gap [46]. The highest intensity peak of the band to band recombination spectrum usually indicates the bandgap of the semiconductor.

1.10.5. Defects

The perovskite lattice structure may have defects which are oxygen vacancies, Vo. The oxygen deficiency of perovskite materials relies on three factors: temperature, pressure, and oxygen partial pressure [47]. It occurs when excited electrons get trapped at Vo which affects the structure of semiconductors, and the optical and electronic properties as well.

1.10.6. Self-trapped excitons

The self-trapped exciton (STE) is one of the excited states in alkaline earth metal titanates [48]. Electronic energy states might be formed within the band gap at the solid surface which is different from the semiconductor bulk [47]. These energy levels can trap holes and electrons as well. Emission from self-trapped excitons in semiconductors can occur from the low to at least room temperature [48]. In this case, the excited electron and hole create a localized distortion in the lattice which lowers their total energy and allows self-trapping to occur due to the breaking of symmetry. The energy that is emitted from a trapped electron is larger at the surface than in the bulk because a trapped exciton is more likely to occur at the surface [48]. Luminescence resulting from the STE recombination was observed in TiO_2, $BaTiO_3$, $SrTiO_3$, and other titanates; this luminescence originates in the TiO_6 octahedron [45].

1.10.7. Photoluminescence Quenching

Fluorescence quenching is defined as a process that decreases the emission intensity of a given substance. Different processes can result in quenching such as excited state reactions, energy transfer, complex formation, and collisional quenching [49]. Semiconductors have variable surface properties which affect their electric and optical properties. For example, defects that are induced at the surface could make electronic states within the band gap that trap the excited electrons from conduction band or excited holes from valence band this trapping could quench the PL [47]. Moreover, adsorbates that are present during the reaction can reduce the intensity of PL [49].

2. Experimental

2.1. Materials

Nanocrystalline calcium titanate ($CaTiO_3$) and silver nitrate ($AgNO_3$) were purchased from Sigma- Aldrich. The particle size of nanocrystalline $CaTiO_3$ was reported by the manufacturer at <100 nm with a surface area around 6.21 m^2/g. Glycerol, silver (I) fluoride(AgF), titanium (IV) isopropoxide (TIPT), acetylacetone (ACA), lauryl amine hydrochloride (LAHC), and calcium nitrate tetrahydrate were bought from Acros.

2.2. In-situ photocatalysis with nanocrystalline $CaTiO_3$ for hydrogen production with sacrificial donor

The in-situ photocatalytic hydrogen generation experiment was set up as in Figure 2.1. The photocatalytic testing was conducted in a closed gas quartz vessel at room temperature. 0.04 g of calcium titanate was suspended in 15 ml distilled water with 10% vol glycerol as an organic sacrificial donor, and then $AgNO_3$ (0, 0.5×10^{-3}, 1×10^{-3}, and 2×10^{-3} M) was added as a cocatalyst precursor. Prior to the reaction, the suspension was mixed in an ultrasonic bath for 15 mins, and then the air was removed by vacuum for 20 mins with argon bubbling in dark environments to decrease oxygen content. The reaction was conducted by exposing the suspension, which is mixed during the reaction with a magnetic stirrer, to a medium pressure mercury lamp (450 W). Then, hydrogen was collected every 20 mins of illumination by passing Ar gas to the vessel at flow rate 40 ml/min. A hydrogen sensor, model 4101-07 from Sierra Monitor, was used to detect hydrogen gas while simultaneously oxygen gas was passing to the sensor at a constant rate 10 ml/min.

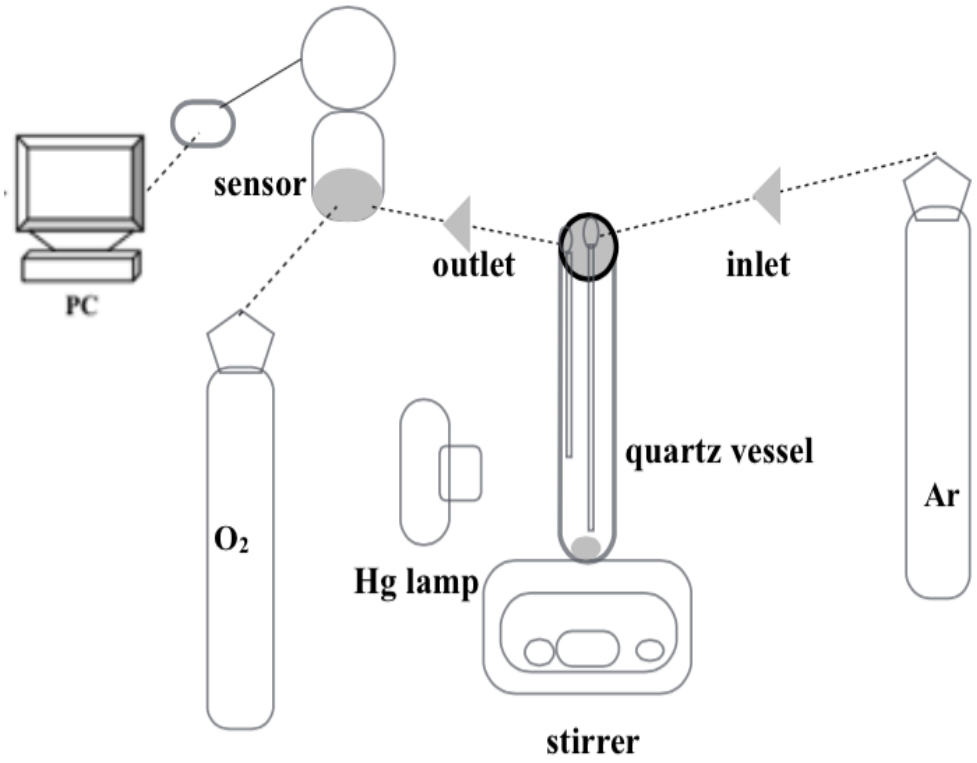

Figure 2.1. The in-situ photocatalytic hydrogen production experiment set up.

2.2.1. In-situ photochemical synthesis of colloidal Ag nanoparticles

The UV-vis spectra of colloidal Ag NPs were determined by using a UV-vis Cary 5000 from Agilent. Colloidal Ag was prepared by mixing 3.5 ml water with 10% vol glycerol to achieve 2 x 10^{-3} M $AgNO_3$ solution. Then, the mixture was degassed by bubbling argon gas for five mins. After that, the absorbance of the colloid solution was measured every 2.5 mins of illumination from the mercury lamp with using a magnetic stirrer to mix the colloid at a different time (0-30 mins).

2.3. Raman spectra

Raman spectra were collected at room temperature using an XPlora confocal microscope from Horiba Scientific, which is equipped with the laser at 532 nm, grating 1200 g/mm, and with a cut-off optical filter at 50 cm^{-1}.

2.4. Diffuse reflectance spectra

The UV-visible diffuse reflectance spectra, UV-vis DRS were measured at room temperature using a UV-vis Cary 5000 from Agilent equipped with the Praying Mantis attachment from Harrick Scientific. Ground $BaSO_4$ of 99.998 % purity from Alfa Aesar was used as a white reference in the UV-vis DRS measurements.

2.5. Photoluminescence spectra

A Fluorolog-3 spectrometer (Horiba) was utilized to determine emission and synchronous PL spectra at room and cryo (LN_2 77K) temperatures. For datasets with multiple peaks, numeric curve-fitting of the photoluminescence spectra was conducted using the Origin 2015 program. The fitting was obtained in these steps (1) analysis, (2) peaks and baseline, and (3) multiple peak fitting.

2.5.1. PL emission spectra

2.5.1.1. The emission spectra of pure $CaTiO_3$

The emission spectra of pure nanocrystalline $CaTiO_3$ were obtained at cryo temperature (77K) by filling quartz test tube 5 mm diameter, from Wilmad Labglass, with the sample. Then, the sample was excited at different λexc ranging from 300 nm to 380 nm to obtain λem ranging from 300 nm to 600 nm with optical slit 3 nm, and time of integration 0.1 s.

2.5.1.2. The emission spectra of Ag/$CaTiO_3$ composite material

First, the suspension was prepared as in our photocatalysis experiment in a quartz flask (500 ml) by adding 350 ml water, 1 g $CaTiO_3$, and 10% vol glycerol, and at [Ag^+] = 1 x 10^{-3} M. After that, the suspension was irradiated with the Hg lamp for 5 hours. The suspension was centrifuged and washed with water to remove any excess organic donor and any metal cations. Then, the composite was dried in vacuum. Finally, the dried sample (placed in a quartz test tube 5 mm in diameter) was scanned at the same setting as pure $CaTiO_3$.

2.6. The in-situ PL emission spectra

First, 0.01 g of $CaTiO_3$ was added to water and 10% vol glycerol in water in a 3.5 ml quartz cuvette. Then, the suspension was outgassed by bubbling argon for at least 5 mins. The cuvette was closed with a stopper, then was placed in small beaker (50 ml), and mixed using stir bar while liquid nitrogen was poured into the beaker until the sample became frozen. Finally, the PL emission spectra were collected at the following settings: optical slit width 1 nm, and the integration time 0.1 s.

2.7. Synthesis of mesoporous $CaTiO_3$

Mesoporous perovskite calcium titanate (meso $CaTiO_3$) was synthesized by a sol-gel process with the aid of a structure-directing surfactant under mild conditions. This synthesis was based on a published procedure [13]. An ACA/TIPT solution was prepared by adding 2.00 g of ACA to 5.68 g of TIPT. Lauryl amine hydrochloride (LAHC) solution was prepared by dissolving 1.10 g in 50 ml of ethanol (Pure 200 proof). Then, 4.72 g of $Ca(NO_3)_2$:$4H_2O$ was added to the LAHC solution with continuous stirring to obtain clear solution of LAHC/$Ca(NO_3)_2$:$4H_2O$. Afterward, the LAHC/$Ca(NO_3)_2$:$4H_2O$

solution was slowly dropped into the ACA/TIPT solution while stirring continuously to obtain the ACA/TIPT/LAHC/$CaTiO_3$ solution with a LAHC-to-TIPT molar ratio of 0.25:1 and a Ca-to-Ti molar ratio of 1:1. Next, the resultant mixture was incubated at 80^{o}C for two days to obtain a complete gel formation. The resulting gel was further dried at 80^o C for two days. Finally, the dried gel was calcined at 600^o C, and after reaching 600^o C, it was kept at this temperature for 4 hours to remove the surfactant and any remaining solvent from the dried gel to yield the mesoporous-assembled $CaTiO_3$ photocatalyst.

2.8. Nitrogen physisorption

The nitrogen physisorption experiments were carried out in Autosorb 1C setup (Quantachrome). The sample was thermally preheated at 200^o C for 8 hours. The physisorption measurement was performed at the boiling point of liquid nitrogen (77K). The surface area was determined according to the BET (Brunauer-Emmett-Teller) equation. The pore size distribution was obtained by the BJH (Barrett-Joyner-Halenda) method.

2.9. In-situ photocatalysis with mesoporous $CaTiO_3$ for hydrogen production without donor

The experiment was set up as in section 2.2. Calcium titanate was suspended in 15 ml distilled water, and then AgF (0, 0.5 x 10^{-3}, 1 x 10^{-3} M, and 5 x 10^{-3} M) was added as a chemical precursor of the cocatalyst. The hydrogen was collected after every 20 mins of illumination by passing Ar gas to the photocatalytic vessel at flow rate 40 ml/min. The hydrogen sensor was used to detect hydrogen gas rate while oxygen gas was passing through the sensor at constant rate 10 ml/min.

2.10.1. The PL emission spectra of mesoporous $CaTiO_3$

2.10.1.1 As prepared mesoporous $CaTiO_3$

The emission spectra of as-prepared mesoporous $CaTiO_3$ were obtained at room temperature (25^o C) by filling a 0.5 mm quartz cuvette with the sample. Then, the sample was excited at different λexc ranging from 320 nm to 420 nm to obtain λem ranging from 300 nm to 650 nm with an optical slit width of 2 nm, and time of integration 0.1 s.

2.10.1.2 Dried mesoporous $CaTiO_3$

We prepared dried calcium titanate by drying as prepared mesoporous $CaTiO_3$ in the oven at 110^o C overnight, and then we measured its mass and collected PL spectra with the same settings listed in 2.10.1.1.

2.10.1.3. Hydrated mesoporous $CaTiO_3$

The hydration of mesoporous $CaTiO_3$ in a 0.5 mm quartz cuvette was conducted in water vapor in a desiccator filled with liquid water, the sample was placed in a tray above the water level, and the desiccator was closed. The hydration occurred overnight, for 2 or 5 days [50]. After the hydrated sample was taken out of the desiccator, the change in mass of mesoporous $CaTiO_3$ was determined gravimetrically, and then the emission spectra were measured at the same setting listed in 2.10.1.1.

2.10.2. Synchronous PL spectra

The synchronous PL spectra were obtained at different Δλ from 30 nm to 100 nm to obtain the optimal Δλ. The slit width was 2 nm, and the time of integration was 0.1 s for all three samples.

2.11. **Figures**

The lattice structure (Figure 1.2) was drawn using Crystalmaker program, and other Figures were drawn by the Origin 2015 program.

3. Results and discussion

3.1. The multi-spectroscopic characterization of nanocrystalline $CaTiO_3$

3.1.1 Raman spectrum

Since calcium titanate has three different structures: tetragonal, cubic, and orthorhombic, and each structure has different properties, we first investigated the crystal structure of our nano- crystalline $CaTiO_3$ semiconductor. From a spectroscopic analysis using Raman spectroscopy, the vibrational modes of calcium titanate were determined. Figure 3.1 shows the Raman spectrum of the $CaTiO_3$ sample at room temperature, and the 11 peaks are attributed to the orthorhombic structure with space group Pbnm which agrees with the literature [19].

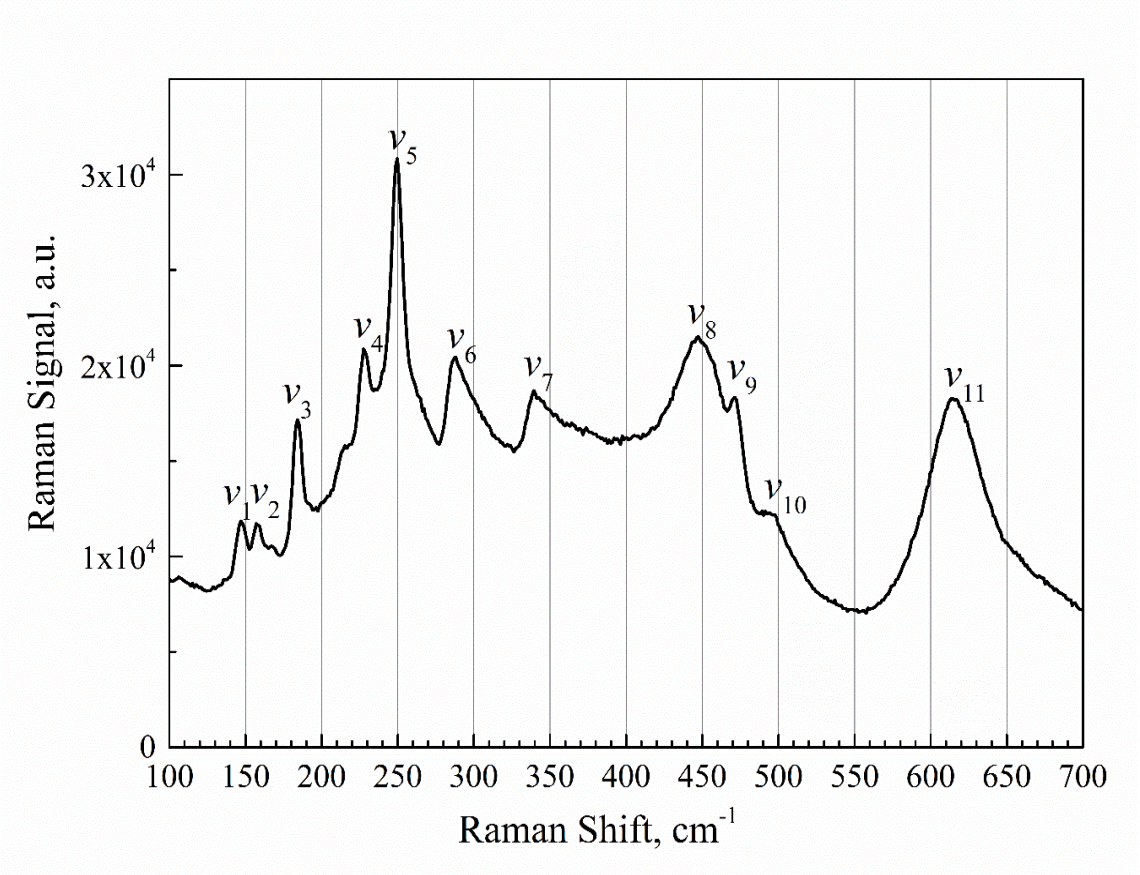

Figure 3.1. Raman spectrum of nanocrystalline $CaTiO_3$.

Orthorhombic $CaTiO_3$ exhibits 24 Raman active modes represented by 7Ag+ 5 B_1 g + 7 B_2 g + 5B_3g. However, some of these bands may not be seen due to low polarizability, or they might overlap with more intense bands. According to Cavalcante et al. [51], the position of the Raman band could be shifted depending on the method used to prepare the material.

From Figure 3.1 above, there are bands at 149, 160, 180, 226, 247, 270, 337, 470, and 620 cm^{-1} which were attributed to different modes (Table 2). These Raman peaks could be assigned depending on symmetry analysis to the seven Ag modes. The bands at 247 and 470 correspond to B_2 g while 494 cm^{-1} attributed to B_1 g [18].

Table 2. Band assignments of nanocrystalline $CaTiO_3$ [18]

Peaks	Raman shifts	Band assignments	V modes
v_1	148 w	Ca^{2+}	vibration of the cation
v_2	158 w	$CaTiO_3$	lattice mode
v_3	180 s	O-Ti-O	Bending
v_4	225 s	O-Ti-O	Bending
v_5	247 vs	O-Ti-O	Bending
v_6	283 m	O-Ti-O	Bending
v_7	337 m	O-Ti-O	Bending
v_8	447 s	O-Ti-O	Bending
v_9	471m	Ti-O_3	torsional mode
v_{10}	495 w	Ti-O_3	torsional mode
v_{11}	620 m	Ti-O	symmetric stretching

w: weak; m: medium; s: strong; vs: very strong

3.1.2 UV-vis diffuse reflectance spectroscopy

Diffuse reflectance spectroscopy (DRS) was utilized to examine the light absorption ability of nanocrystal calcium titanate by measuring its ability to reflect light. Figure 3.2. shows the reflectance (R%) of the material in the wavelength range from 275 nm to 800 nm.

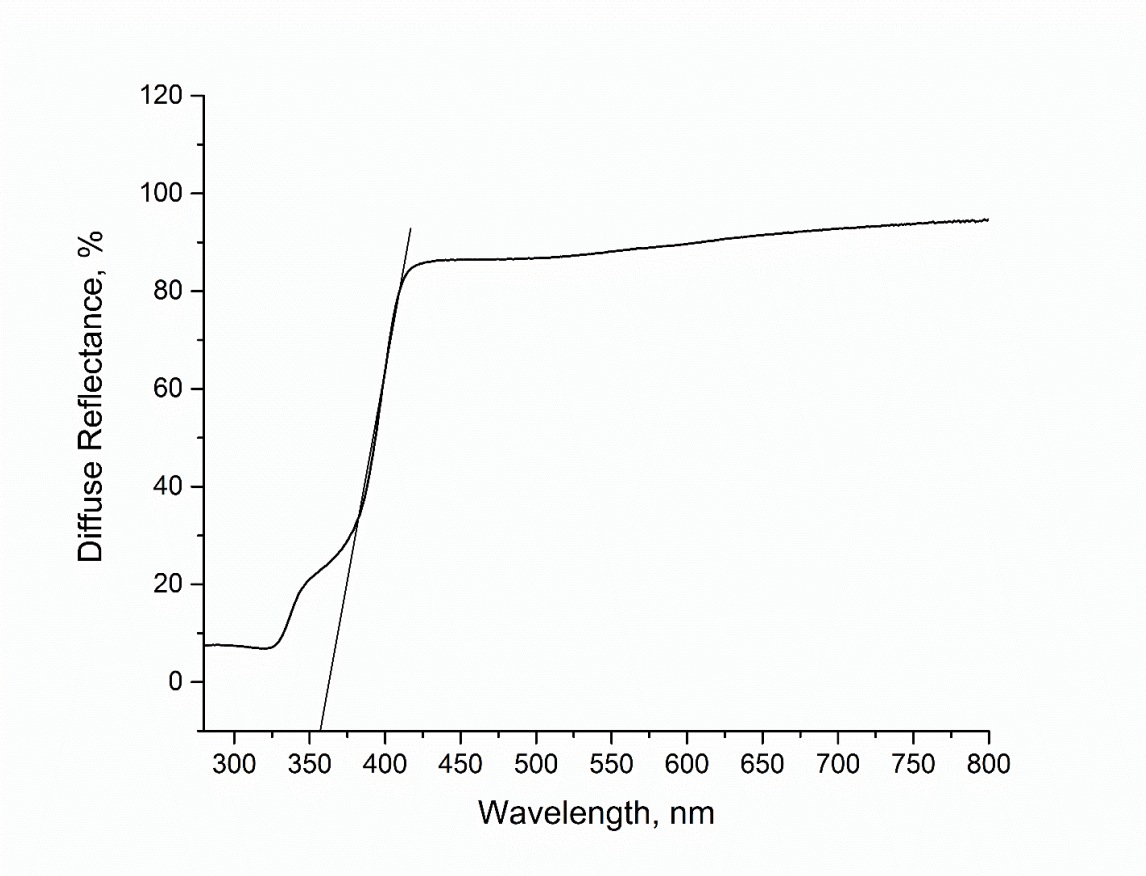

Figure 3.2. UV-vis DRS spectrum of nanocrystalline calcium titanate.

It clearly can be seen that the absorption edge of $CaTiO_3$ appeared in the UV light range around 360 nm. However, this method is not accurate to determine the band gap energy of the semiconductor. Therefore, the band gap energy was determined by converting the reflectance (%) to absorption using the Tauc plot method via a modified Kubelka-Munk method.

In the Tauc plot method, the reflectance (vertical axis) is plotted as $(F(R)\ h\nu)^{1/n}$ while the absorption wavelengths (horizontal axis) are recalculated to the photon energy hν (eV) by the following equation: $h\nu = 1240/\lambda$. Since orthorhombic $CaTiO_3$ has direct allowed transition as reported by Lee at el. [6], n = 1/2 was used for our semiconductor. Figure 3.3 depicts the Tauc plot used to determine the direct band gap of our sample. In Figure 3.3, the line drawn corresponds to the point of inflection on the curve, and the hν value at the point of intersection of the horizontal axis is the direct band gap Eg value.

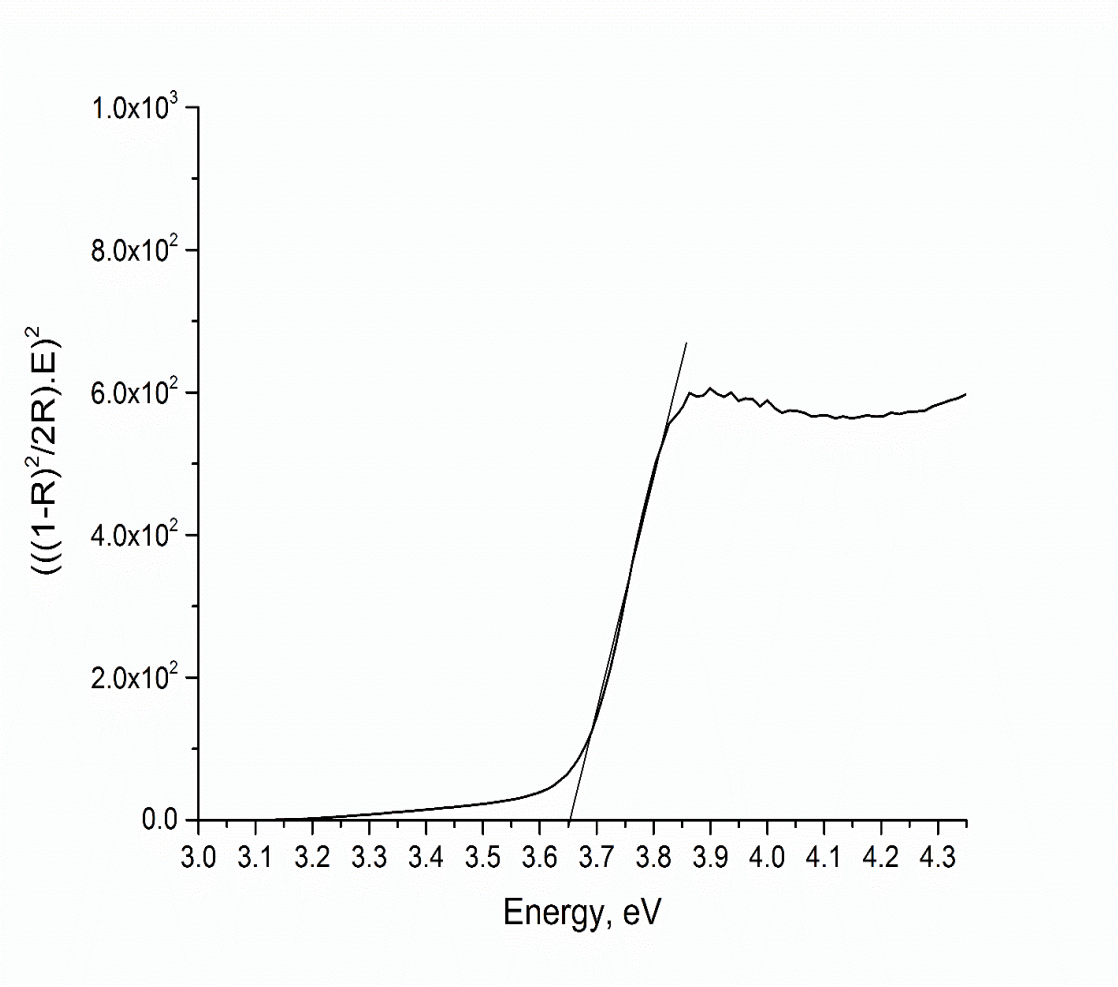

Figure 3.3. The Tauc plot of the direct band gap of nanocrystalline calcium titanate.

We found that the direct band gap of nanocrystal $CaTiO_3$ is approximately 3.65 eV (340 nm). Therefore, it can be noticed from the light absorption ability of orthorhombic $CaTiO_3$ that it can absorb only UV light with a wavelength shorter than 400 nm [52].

3.1.3. Photoluminescence of pure $CaTiO_3$

Photoluminescence spectroscopy has been utilized to study the structure, the combination of electrons and holes, and to identify defects or impurities in the semiconductors [16]. When the calcium titanate sample is illuminated with a monochromatic illumination source, some of this light may be absorbed to create electron/hole pairs. It is known that many of the electron/hole pairs emit photons upon relaxation, and most photons are Rayleigh scattered.

First, an empty quartz test tube 5 mm in diameter was scanned at different excitation wavelengths to measure its PL emission spectra at the same settings as those used to measure the pure nanocrystalline calcium titanate PL emission; as expected, no emission was detected. Then, we measured the PL emission of our sample at cryo temperature (77K) to obtain the high-intensity PL. Figure 3.4 shows the PL emission spectra of pure $CaTiO_3$ that was excited at different excitation wavelengths ranging from λexc = 300 nm to λexc = 350 nm with a slit width of 3 nm and an integration time 0.1 s. A set of bands was recorded at different wavelengths, and the position of each band red shifts with increasing excitation wavelength. The intensity of the bands increased gradually and reached the maximum signal intensity at λexc = 320 nm, which is an extra band gap excitation (at ca. 3.5×10^5 a.u. at the maximum). Then the intensity started to decrease around the band gap 3.63 eV (340 nm) and sub-band gap until it showed the lowest intensity at λexc = 350 nm.

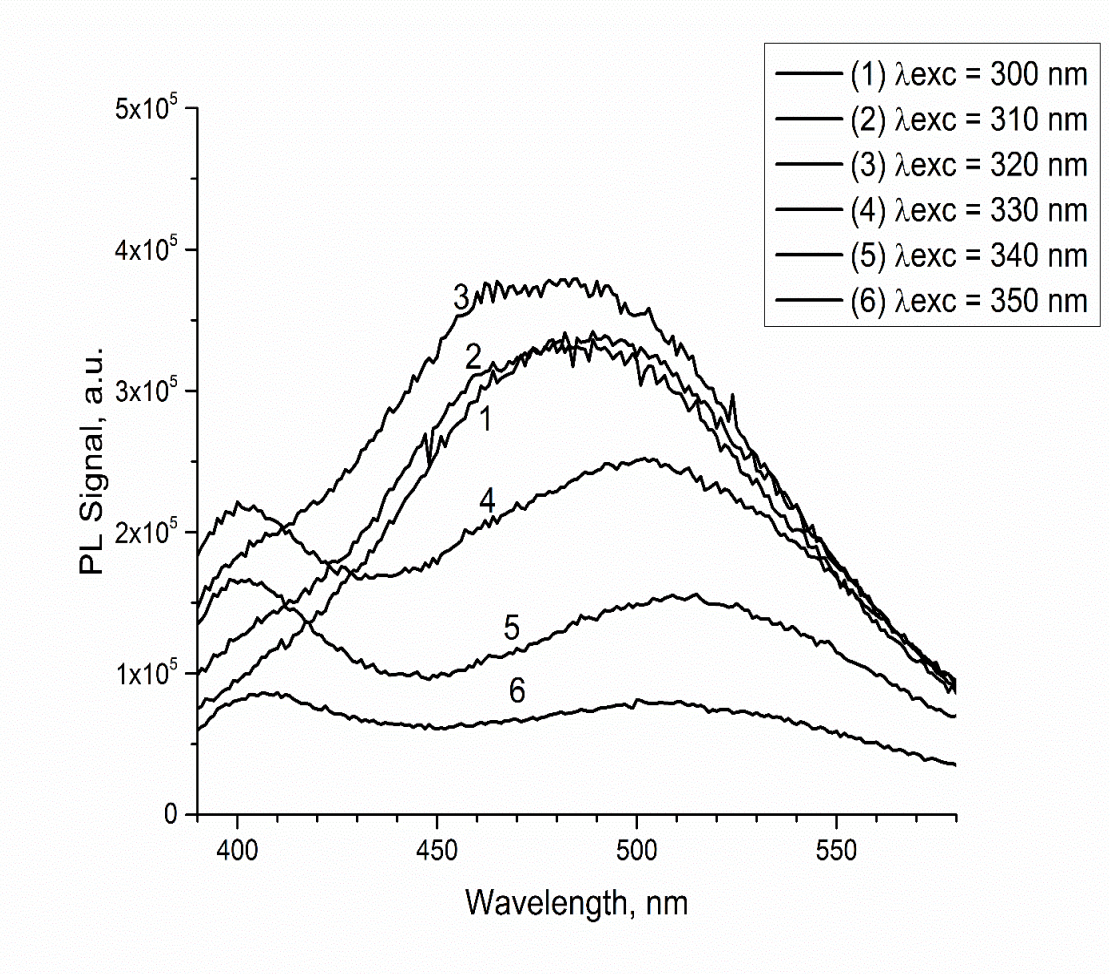

Figure 3.4. The photoluminescence spectra of nanocrystalline $CaTiO_3$ at 77 K.

Like $SrTiO_3$ and $BaTiO_3$, the filled states in the valence band of $CaTiO_3$ are derived from oxygen 2p orbitals, while the empty states in the conduction band are derived from Ti 3d orbitals [44-53]. When $CaTiO_3$ absorbs radiation energy larger than the band gap at 3.65 eV (340 nm), the UV absorption corresponds to charge transfer between O^{2-} to Ti^{3+} localized within the TiO_6 octahedron [43]. Further, in the visible region, the photoluminescence emission results from the interaction between small polarons which are formed by excited electrons with holes to form self-trapped excitons (STE) [44].

Figure 3.5 shows the photoluminescence of nanocrystalline $CaTiO_3$ excited at the extra-band gap energy (320 nm). The peak at 405 nm was attributed to a defect from oxygen vacancy which is located near the conduction band minimum [6]. A broad emission band with a maximum in the visible region around 470 nm was also observed, and this was assigned to the recombination radiation of the self-trapped exciton of octahedral $(TiO_6)^{8-}$ group [54,55]. The shoulder around 510 nm was assigned to a second self-trapped exciton which was also reported for $SrTiO_3$ [44] and which results from the recombination of excited electrons and holes in delocalized states.

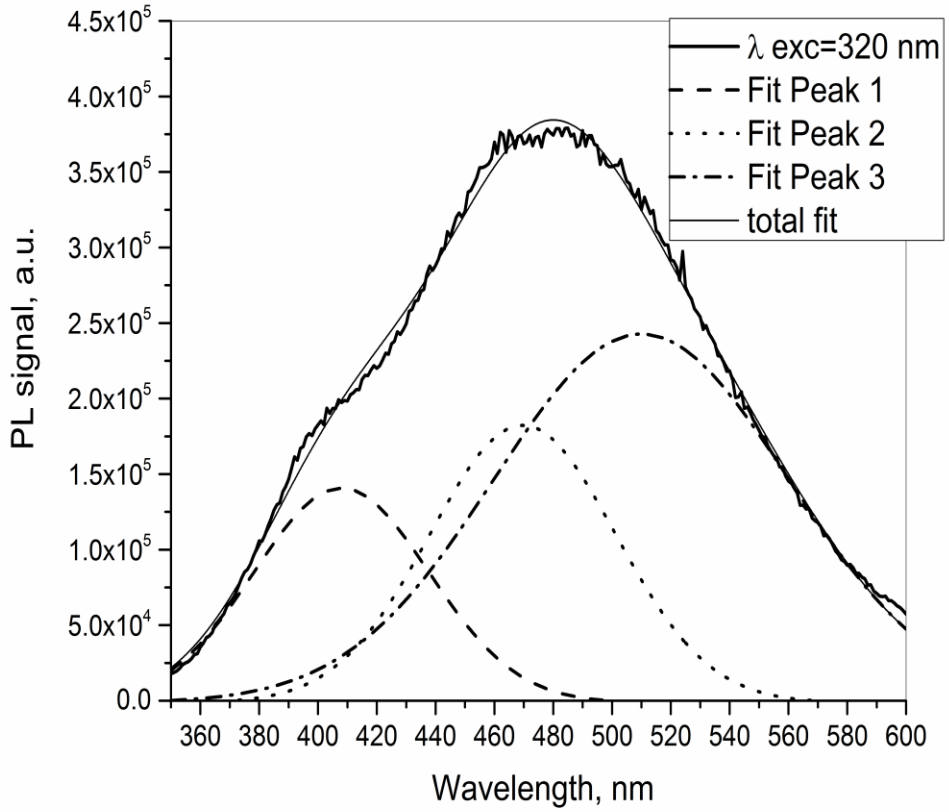

Figure 3.5. The PL emission spectrum of calcium titanate obtained at λexc = 320 nm at 77 K.

We also performed numeric fitting of peaks of $CaTiO_3$ in the spectrum in Figure 3.5 via a multi-Gaussian function. All three peaks (405 nm, 470 nm, and 510 nm) were fitted with Gaussian peaks, and the fourth broad curve corresponds to the spectral background. The parameter of each peak is indicative of the respective transition. The fitted peaks have the following parameters: 1) the peak at 405 nm (3.02 eV) with the FWHM = 68 nm, 2) the peak at 470 nm (2.64 eV) with the FWHM = 74 nm, and 3) the peak at 510 nm (2.42 eV) with the FWHM 118 nm. We proposed a scheme (Figure 3.6) for the observed photoluminescence in $CaTiO_3$. We identified possible defects and excitons in our photocatalyst which would be useful to study photocatalytic activity later.

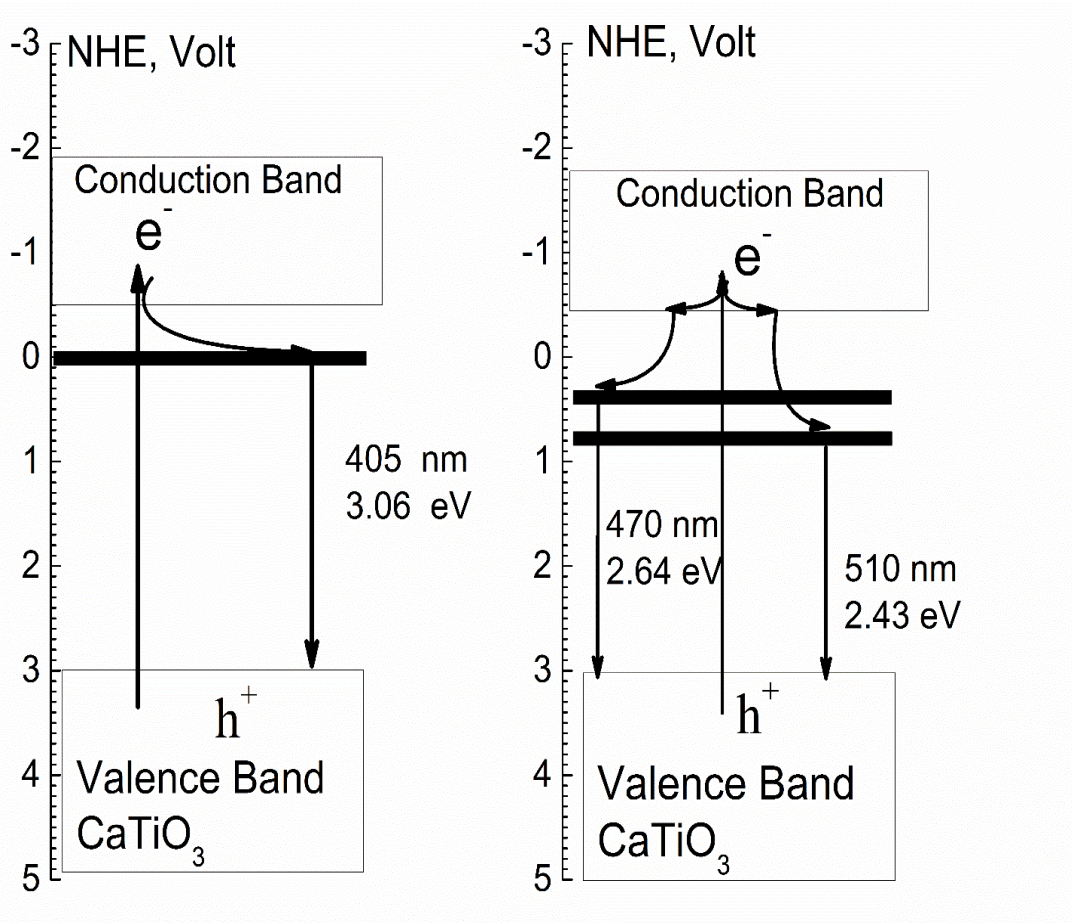

Figure 3.6. A proposed scheme for the photoluminescence emission in $CaTiO_3$

3.2.1. The in-situ photochemical reaction of the $AgNO_3$ precursor to form metallic Ag nanoparticles (Ag NPs)

From the in-situ photoreduction of Ag^+ ions to Ag nanoparticles using a mercury lamp for illumination in the presence of glycerol at room temperature, we noticed that the color of Ag^+/glycerol solution over variable periods of time had changed from colorless to yellow indicating the formation of metallic Ag NPs in the glycerol solution, and we also noticed that the colloid was stable for a week. According to Patel et al. [56], glycerol is able to reduce Ag^+ ions to Ag^0 under microwave radiation, and the colloid was stable even without adding stabilizer which agrees with our observation.

In our experiment, the formation of Ag NPs was investigated by UV-vis spectroscopy, which is considered a useful tool for the detection of produced nanoparticles (NPs) over different time. The UV-vis spectra in Figure 3.7 depict the formation of colloidal silver, and the metallic Ag NPs can be identified by a Surface Plasmon Resonance (SPR) peak at around 410 nm with a small red-shift in the wavelength of the peak that could be related to Ag NPs of different sizes [37]. Moreover, the absorbance of the SPR peak increased as the reaction time increased, which can be attributed to the continued reduction of the silver ions and increase the concentration of metallic Ag NPs. However, after exposure for 27.5 mins, the Ag NPs obtained showed a UV-vis absorption peak with a maximum value centered at 425 nm. When the reaction time reached 30 mins, the absorbance stopped increasing, and the λmax value was slightly blue-shifted to 420 nm.

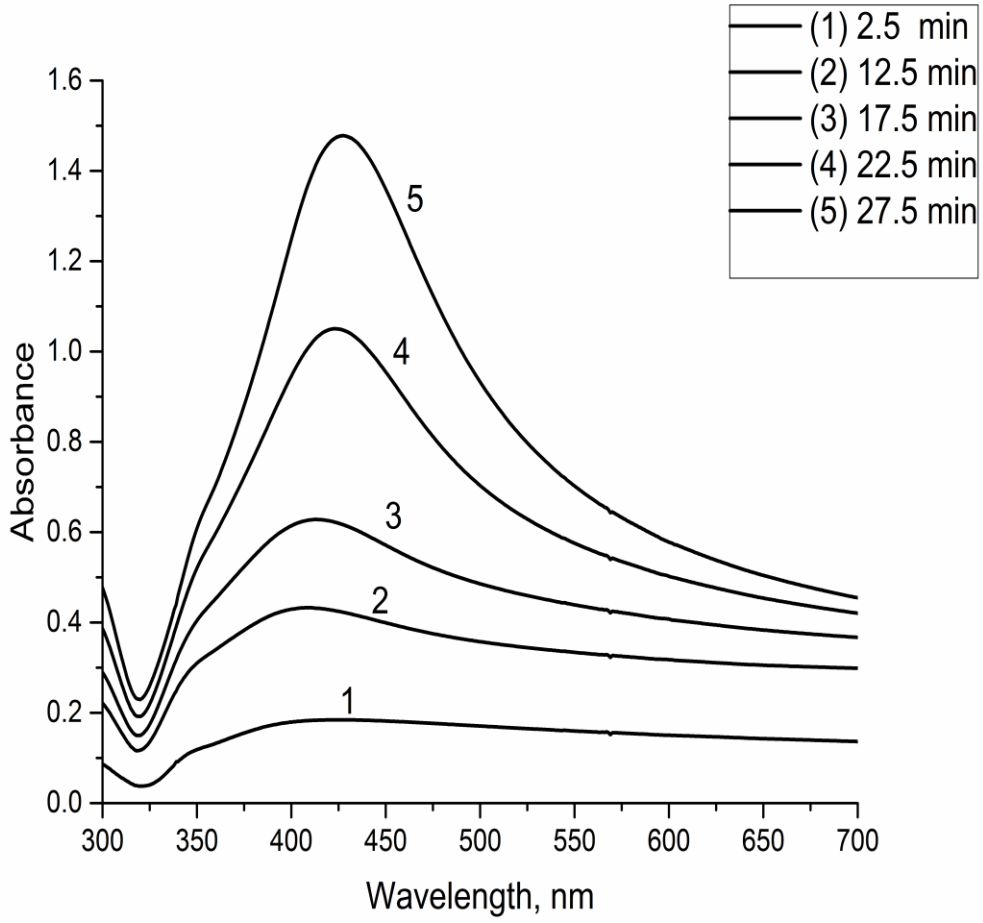

Figure 3.7. UV-vis spectra of colloidal Ag NPs at variable exposure time to the UV light.

It can be clearly seen that there is a peak around 410 nm which is a plasmonic maximum. There is also an absorbance at 500 nm in the spectra, and this probably due to the aggregation of different size of Ag NPs [56]. Further, silver nanoparticles (Ag NPs) exhibit UV light absorption at ca. 340 nm due to the interband transition from 5s to 5p orbital [36].

Since the blue or red shifts of the SPR band and FWHM depend on the nanoparticle size [38], we applied numeric curve fitting of the peaks via multiple-Gaussian function for the UV-vis spectrum at 15 mins of illumination (Figure 3.8, top) and the spectrum with the

maximum value at 27.5 mins of illumination (Figure 3.8, bottom). The two peaks in the UV-vis spectrum at 15 min of exposure (410 nm and 495 nm) were fitted with multiple-Gaussian peaks. It is hard to exactly fit the small shoulder at 330 nm due to the 5s to 5p transition, we found that the peaks have the following parameters: 1) at 410 nm with FWHM = 84 nm, and 2) at 495 nm with FWHM = 221 nm. Further the numeric fitting of the spectrum at 27.5 min indicated the following parameters: 1) at 426 nm = 96 nm, and at 520 nm = 145 nm.

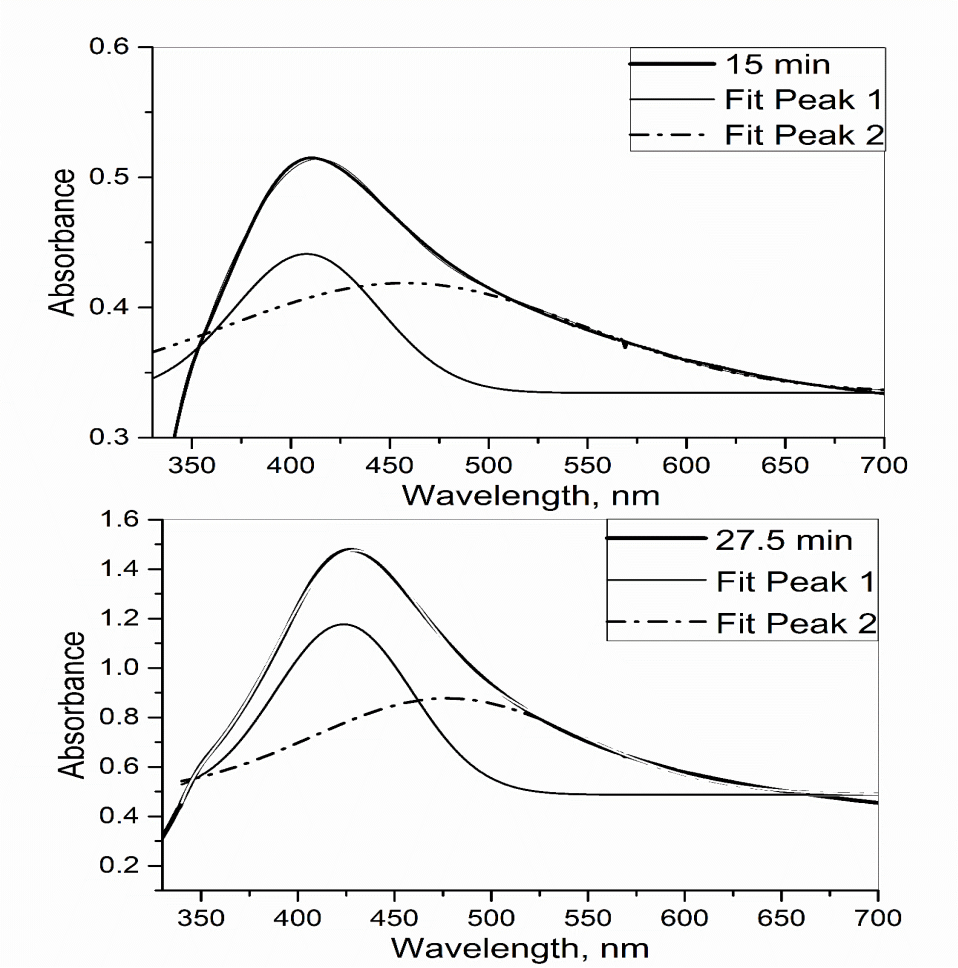

Figure 3.8. UV-vis spectra of colloidal Ag at 15 min illumination (top) and 27.5 min (bottom).

According to theoretical studies, dipolar absorption is related to smaller nanoparticles (< 20 nm) [38], and the ratio of the surface atoms can increase with the decrease of particle diameter. Based on literature spectra [56], the size of Ag NPs in this experiment was between 15-18 nm.

3.2.2. Photoluminescence of silver nanoparticles in colloid solution

A colloidal solution was prepared as described in section 3.2.1, and then it was irradiated with a Hg lamp for 20 min in order to obtain the optimum size of Ag NPs. The photoluminescence spectrum was obtained at room temperature by exciting the 5s to 5p transition at λexc = 350 nm, and λem ranged from 360 nm to 550 nm. Figure 3.9 presents the conventional PL emission spectrum of Ag NPs, and a broad peak central at 450 nm is seen; this peak was attributed to the radiative decay of SPR excited in Ag NPs [52]. It was reported in the literature [37] that Ag NPs with small size (8 nm-11 nm) have two luminescence peaks which result from band to band transition and the SPR luminescence. Further, when the nanoparticle size increases, the intensity of two peaks decreases and peaks blue shift. Based on the observation of the emission PL of Ag NPs in our experiment, it has one peak in the visible region which corresponds to the size of Ag NPs > 11 nm. In Figure 3.9, R indicates the Raman peak of water solvent.

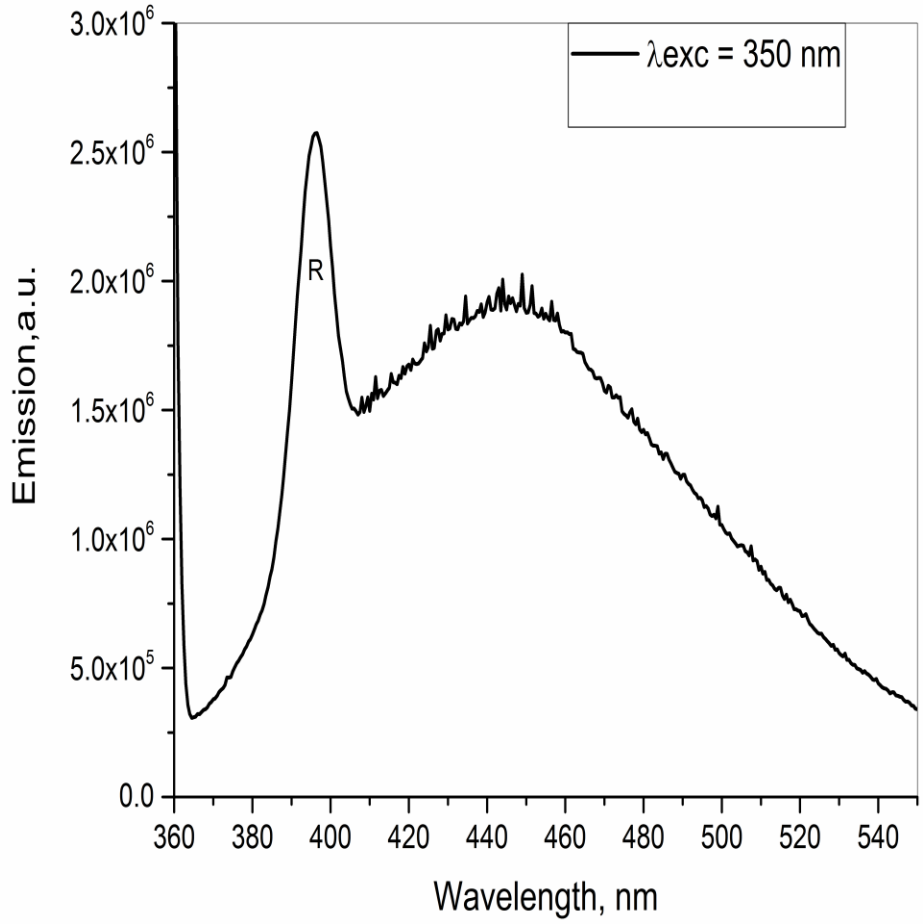

Figure 3.9. PL emission spectrum at λexc = 350 nm of metallic Ag NPs.

Since metals do not have a forbidden energy gap between the conduction band and the valence band, the excited electron can recombine with a hole. However, the excitation of SPR in Ag NPs increases the probability of radiative decay via the photoluminescence [37].

We hypothesized about the process of the PL emission from Ag NPs as shown in Figure 3.10. We assumed that the electron gets excited by the light to its plasmon resonance following by nonradiative relaxation and then radiative decay which contributes to the PL emission.

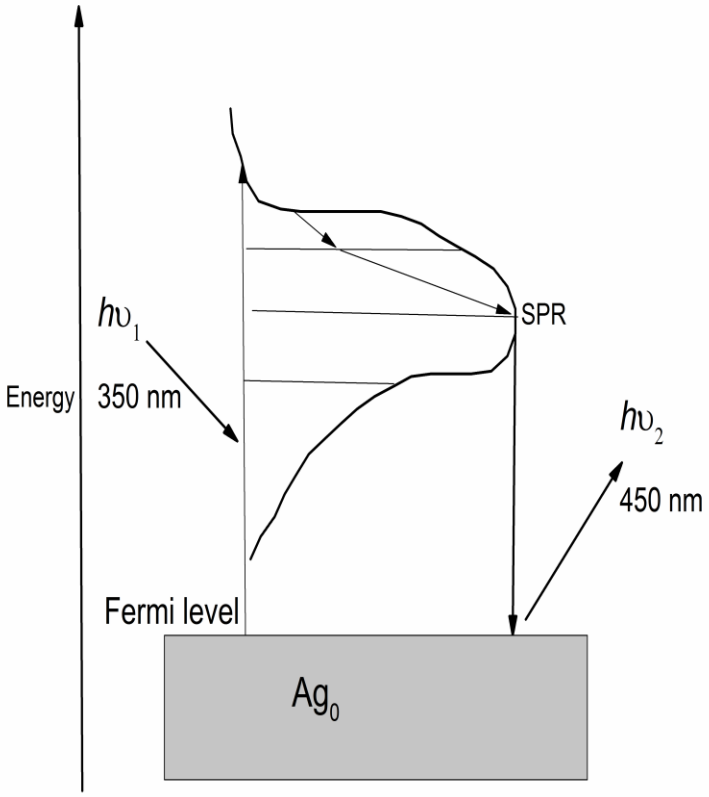

Figure 3.10. The hypothesis of the radiative emission process in metallic Ag NPs.

3.3.1. Photocatalytic hydrogen production with nanocrystalline $CaTiO_3$ and silver promoter, with a sacrificial electron donor.

We started our photocatalytic hydrogen production experiments by testing nanocrystalline calcium titanate in water without an organic donor or metals by exposing the photocatalytic reactor to the full spectrum of the Hg lamp (Figure 3.11). Since the photocatalytic activity of the semiconductor relies on the dosage of the semiconductor in the reaction, we tried to use the optimum concentration of the calcium titanate according to the literature [57]: this optimum concentration is between 30-50 mg/10 ml in order to reach the high activity. We found that the suspension of $CaTiO_3$ produced a trace amount of hydrogen gas (less than 5 μmol/g.h). After that, we examined $AgNO_3$ separately by suspending it in a water/10% vol glycerol solution and exposed to the Hg lamp. There was no hydrogen generation observed, as we expected.

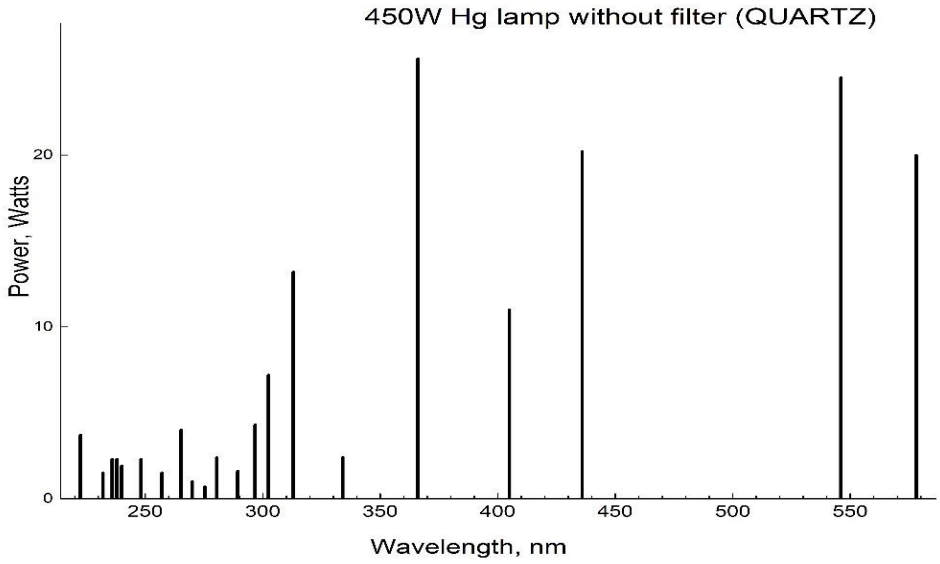

Figure 3.11. Optical spectrum of 450 W Hg lamp without an optical filter taken from "General operating instructions for Ace photochemical U.V. power supplies & mercury vapor lamps".

Next, we investigated the ability of nanocrystalline calcium titanate loaded with Ag NPs in the presence of glycerol as organic donor to generate hydrogen under UV and visible light irradiation. Following our data of photoreduction of Ag^{+}, we ran the in-situ photocatalysis by irritating the suspension under UV light for 20 mins at room temperature. Then, we started to collect the hydrogen generated.

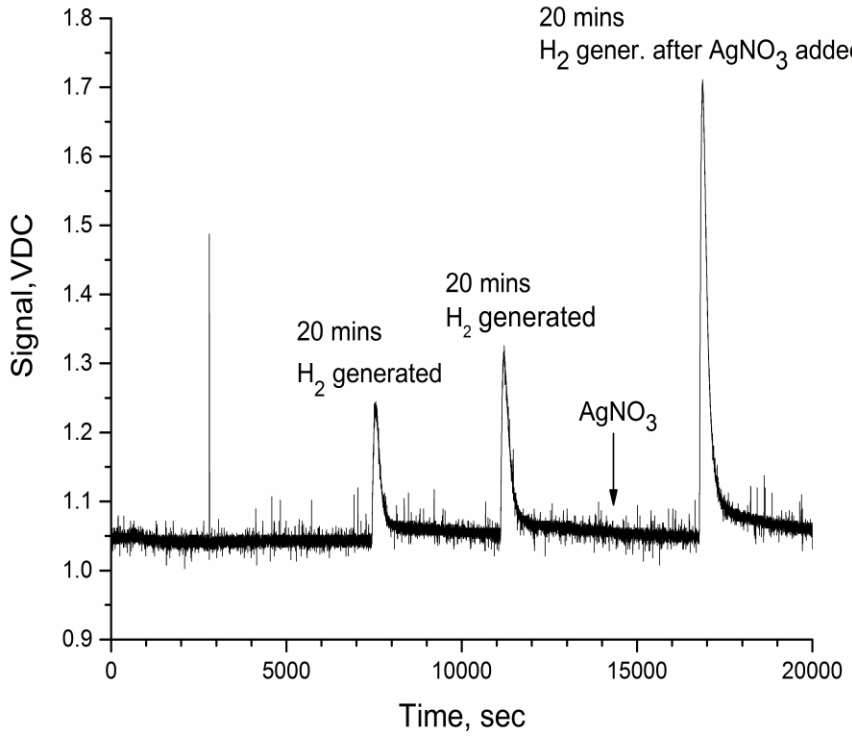

Figure 3.12. Raw data of hydrogen collection obtained by hydrogen sensor.

Figure 3.12 shows the raw data obtained from the hydrogen sensor (1) before Ag^{+} deposited to the semiconductor and (2) when the metal was added to the reaction at the concentration 5×10^{-4} M. In this case, the metal enhanced the photocatalytic activity 2.5 times, and that could be because the transfer of electron from photocatalyst to the metal, Figure 3.13.

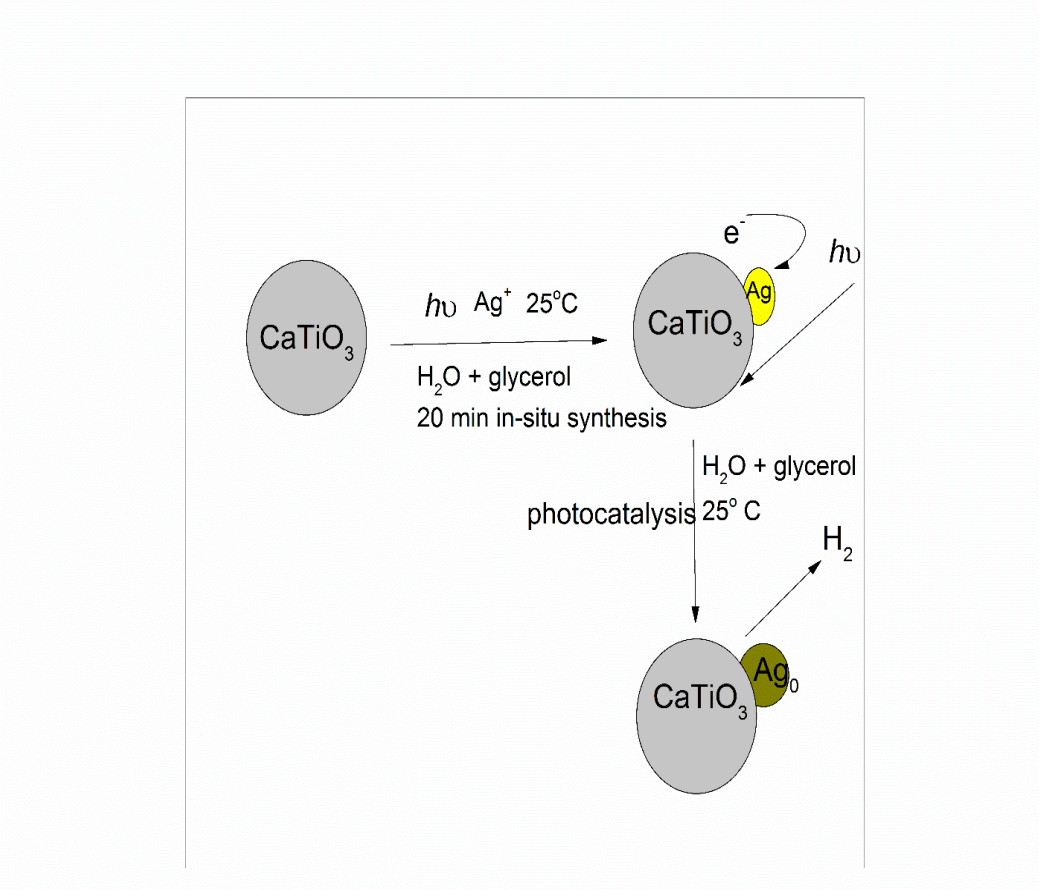

Figure 3.13. In -situ photocatalysis hydrogen production process.

3.3.2. The dependence of photocatalytic rate on the amount of Ag promoter

We found that the photocatalytic activity depends on the amount of silver loaded on $CaTiO_3$ and the type of the excitation light. For example, $CaTiO_3$ showed high activity under UV light ($\lambda \geq 210$ nm) as in Figure 3.11, but it showed less activity under visible light ($\lambda \geq 400$ nm) because the band gap is too high to harvest visible light. Table 3 and Figure 3.14 present the H_2 evolution rates from photocatalytic experiments when different amount of Ag was added. It can be seen that unloaded $CaTiO_3$ produced the minimum amount of hydrogen. Then, when metallic Ag NPs were produced in the photoreaction, the

rate gradually increases until it reached the maximum at $[Ag^+] = 10^{-3}$ M, and then the activity decreased with further increase of the metal amount.

Table 3. The rate of photocatalytic hydrogen production for different concentrations of co-catalyst.

Ag^+ concentration (M)	H_2 Rate (μmol/g.h)
0	56
0.5×10^{-3}	147
1×10^{-3}	167
2×10^{-3}	49

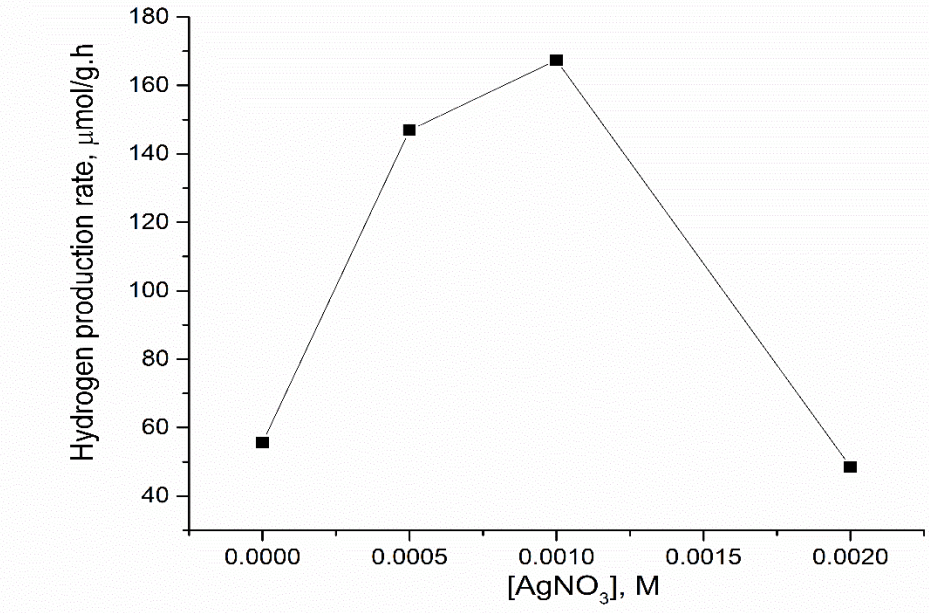

Figure 3.14. The hydrogen production rate (μmol/g.h).

The obtained dependence of the rate upon the concentration of the Ag promoter has a resemblance to the typical bell-shaped curve commonly observed for metal dopants in the photocatalysts [58]. The highest photocatalytic activity was achieved at $[Ag^+] = 1 \times 10^{-3}$ M. At higher concentrations of the deposited metal, the metal would cover the surface of the semiconductor and work as a filter that partially blocks the sites on the surface during the photo-process. When the concentration of the metal is lower than the optimal amount, there are not enough traps of charge carriers in the semiconductor. Further, when the loaded concentration is higher than the optimal concentration, recombination rate between electrons and holes will increase since the distance between charge traps becomes shorter [31].

Upon completion of the photocatalysis, the supernatant was tested for the presence of the unreacted Ag^+ precursor, using the SenSafe® Silver test strips. This strip has the detection range of silver in water at 5 ppb (μg/L) to 100 ppb (μg/L). We noticed the change in the color of the strips after the experiment. Therefore, the majority of Ag^+ precursor in the solution has been photochemically reduced to metallic silver.

Figure S.2. Silver test strips before and after the photocatalytic reaction.

$CaTiO_3$ is not active under visible light but when the metal promoter was added, the experiment showed trace amount of hydrogen (less than 5 μmol/g.h), and this result is consistent with other reported metal dopants [29].

3.4. Studies of charge transfer between silver promoter and calcium titanate semiconductor

3.4.1. The ex-situ PL emission spectroscopy of pure $CaTiO_3$ and dried $Ag/CaTiO_3$ composite.

It was interesting to us after we studied the hydrogen generation from metallic silver loaded on nanocrystalline calcium titanate to study the efficiency of charge transfer using the photoluminescence (PL) spectroscopy. It is well known that the PL mainly results from the recombination of excited electron–hole pairs. Conversely, a lower emission intensity indicates a decrease in the recombination rate [39]. Many studies suggest that metals adhered to the surface of a semiconductor can enhance or quench the PL, depending on the properties of the metal such as its size and shape [59]. Thus, photoluminescence spectroscopy can be used to study charge transfer from semiconductors to metals or vice versa.

A conclusion about the relative amount of charge carriers in the materials can be made by comparing the samples at the same instrumental setting. The intensity of the PL emission was measured at variable excitation wavelengths (310 nm, 340 nm, and 380 nm) for semiconductor-only and composite photo-catalysts at cryo temperature (77 K). We notice that when the semiconductor absorbed the light at the extra-band gap energy, λexc = 310 nm (Figure 3.15 A), the emission spectrum showed a high intensity compared to the other excitation wavelengths. However, it exhibited a broad poorly resolved band with a

maximum peak at 470 nm which was assigned to recombination radiation of self-trapped exciton of octahedral $(TiO_6)^{8-}$ group as we discussed in a previous chapter, 3.1.3. The emission spectrum at the band gap 340 nm has a medium intensity with the better resolved peaks. For instance, the peak at 410 nm (due to a defect from an oxygen deficiency) shows a distinct emission. However, the intensity of emission from the two self-trapped excitons decreased, and the peaks overlapped and red shifted.

When the excitation energy lies in the sub-band gap range, the emission spectrum exhibits a peak with low intensity. The excitation energy used in this case (3.2 eV corresponding to 380 nm) is lower than the band gap (3.63 eV), so it is difficult for an electron in the valence band to be directly excited to the conduction band; however, it could be excited to the localized levels within the forbidden gap [60].

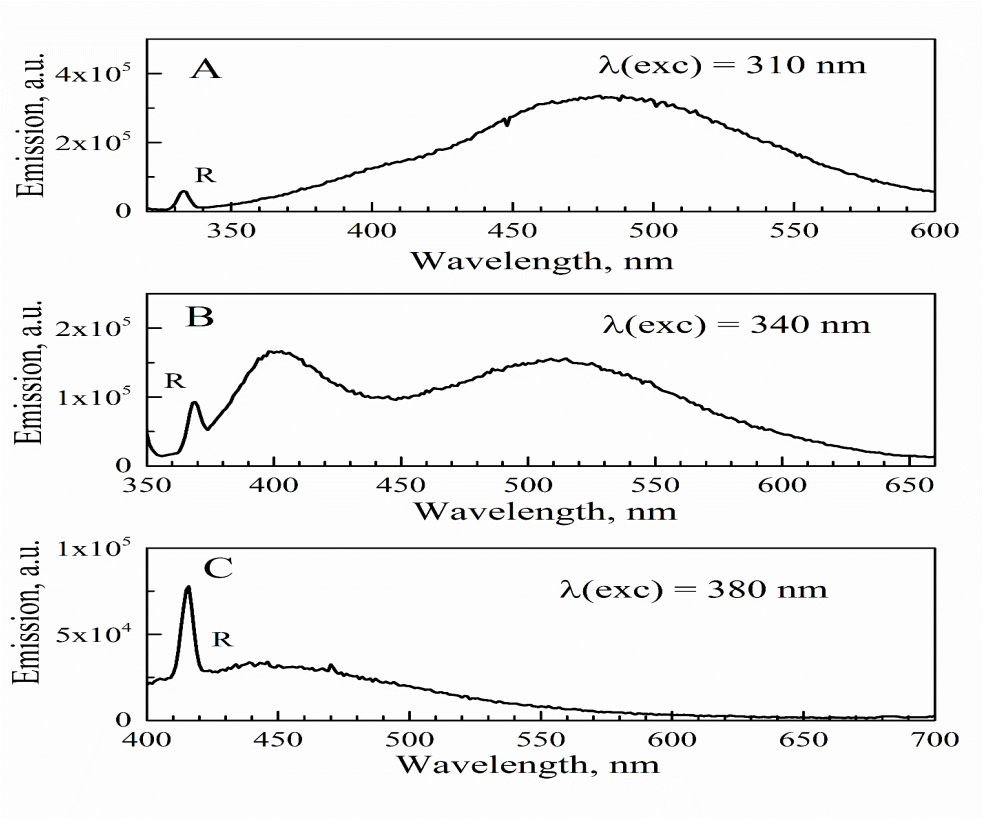

Figure 3.15. The PL emission spectra of pure nanocrystalline calcium titanate.

We had photo-excited an $Ag/CaTiO_3$ composite which was dried in vacuum (Figure 3.16) using the same settings (λexc = 310 nm, 340 nm, 380 nm, with variable λem, and a slit width of 5 nm) that we used for the PL emission spectra of pure $CaTiO_3$ (Figure 3.15).

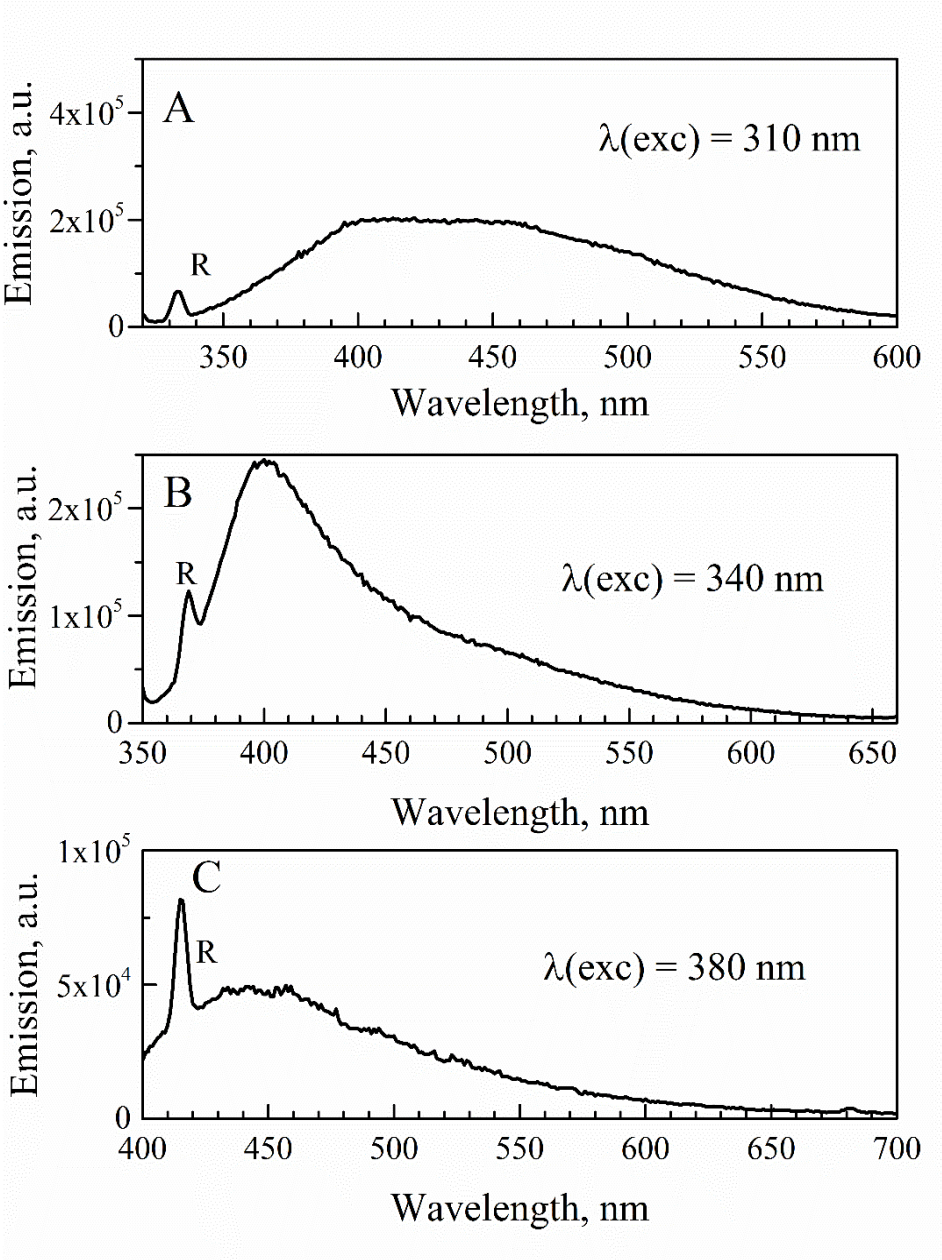

Figure 3.16. PL emission spectra of $Ag/CaTiO_3$ composite.

By comparing, the emission spectrum at the extra-band gap excitation (310 nm) of pure nano- crystalline $CaTiO_3$ (Figure 3.15A) with that of $Ag/CaTiO_3$ composite (Figure 3.16 A), we found that the intensities of transitions due to the two self-trapped excitons (STEs) at 470 nm and 510 nm in $Ag/CaTiO_3$ are much lower in intensity than of the pure $CaTiO_3$. We applied numeric multi-Gaussian fitting to the spectrum of pure $CaTiO_3$ and $Ag/CaTiO_3$ composite. For pure $CaTiO_3$, the fitted peaks have the following parameters: 1) the peak at 405 nm with the FWHM = 44 nm, 2) the peak at 470 nm with the FWHM = 99 nm, and 3) the peak at 510 nm with the FWHM = 126 nm

For the PL spectrum of $Ag/CaTiO_3$ (Figure 3.16 A), the fitted peaks have the following parameters: 1) the peak at 400 nm with the FWHM = 63 nm, and 2) the peak at 454 nm with the FWHM = 70 nm, and 3) the peak at 505 nm with FWHM = 85 nm. Thus, the two peaks corresponding to 466 nm and 505 nm, the STEs, are quenched while there is an enhancement in the intensity around 405 nm. Consequently, we hypothesized that the quenching of the spectra results from the charge transfer from conduction band in the semiconductor to Ag^+ precursor during the photochemical reaction which results in growing the metallic Ag NPs consistently with the proposed diagram in Figure 3.17.

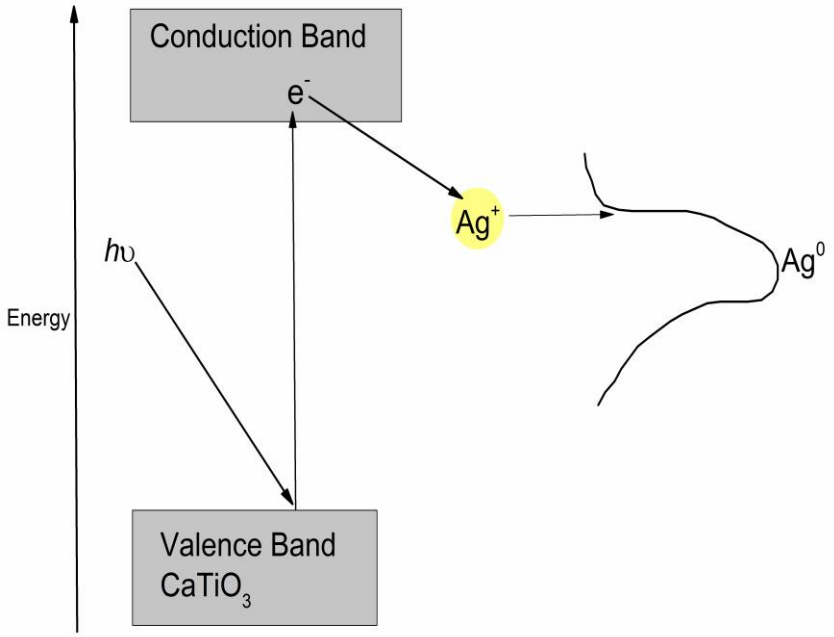

Figure 3.17. Charge transfer from the semiconductor to the metal.

3.4.2. The in-situ PL emission spectroscopy of the Ag/$CaTiO_3$ composite.

We assumed that the PL intensity can be enhanced or quenched due to the electron transfer from semiconductors to metal NPs. To prove this hypothesis, we measured the in situ synchronous PL spectra of the mixtures of Ag^+ with $CaTiO_3$ suspended in water/glycerol.

In this experiment, we measured PL emission spectrum at cryo temperature (77K) for a composite Ag/$CaTiO_3$ sample at $\lambda exc = 350$ nm and $\lambda em = 360$ nm - 550 nm, normalized by the PL emission spectra of $CaTiO_3$, $AgNO_3$ (all samples in situ mixed with glycerol and water). Figure 3.18 shows the PL emission spectrum (solid line) of Ag/$CaTiO_3$ in

glycerol/water sample which appears to be different from $CaTiO_3$ suspended in glycerol/water (dash line). This means that the loading of Ag NPs has reduced the intensity of photoluminescence of the semiconductor. In the PL spectrum of $CaTiO_3$, there are bands with maximum in the visible region at 465nm (2.67 eV), the first self-trapped exciton (STE_1), a shoulder at 505 (2.38 eV), the second self-trapped exciton (STE_2), and another peak at 405 nm (2.97 eV) (oxygen vacancy).

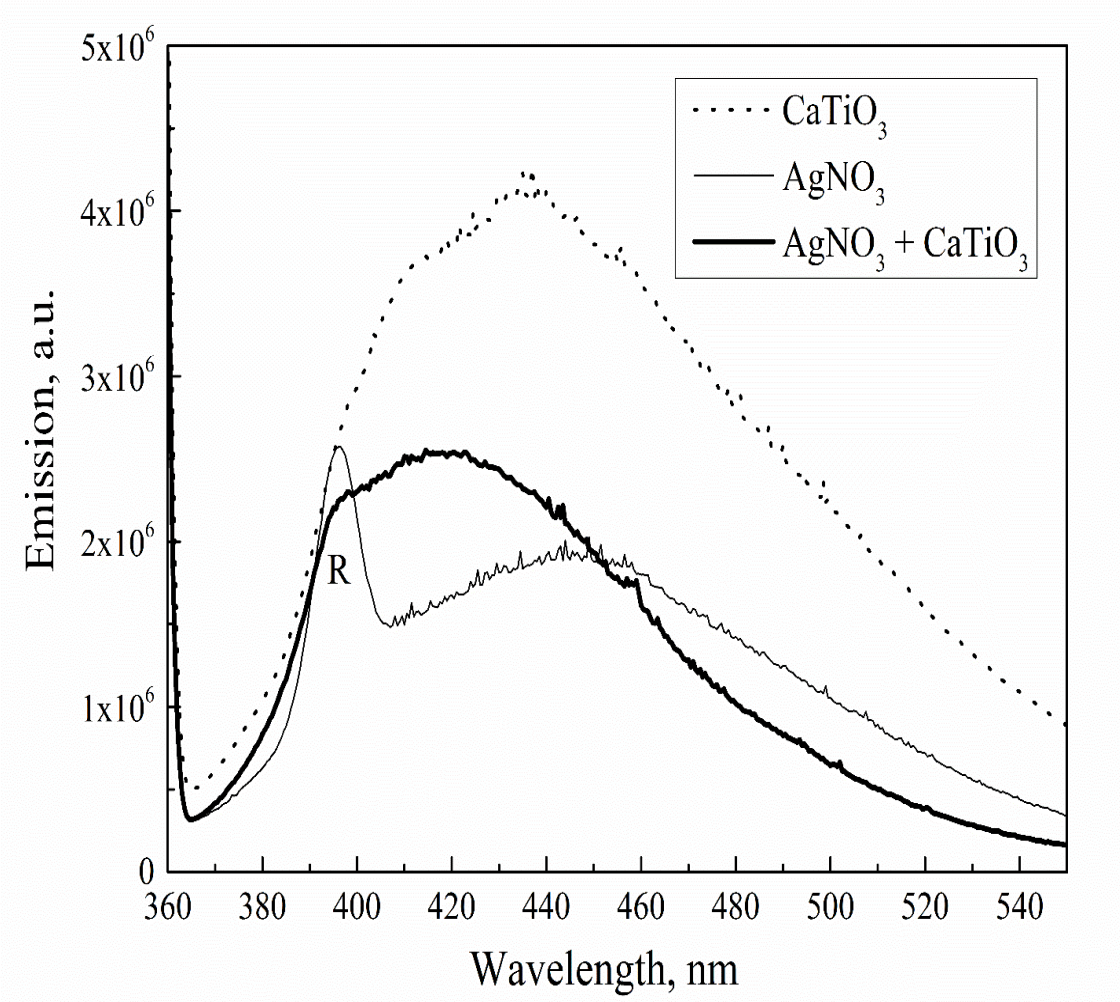

Figure 3.18. The in-situ PL spectra of $Ag/CaTiO_3$, $CaTiO_3$, and $AgNO_3$ obtained at λexc = 350 nm.

The PL quenching factor is calculated by dividing the total intensity of $CaTiO_3$ and the intensity of $AgNO_3$ spectra by the intensity for a composite $Ag/CaTiO_3$ at the same excitation wavelength. For example, the value of the PL quenching at 350 nm was obtained by dividing the PL intensity of the $CaTiO_3$ sample (4. 11 x 10^6 a.u.) + the PL intensity of Ag NPs sample (1.85 x 10^6 a.u.) by the intensity of $Ag/CaTiO_3$ at the same wavelength (2.33 x 10^6 a.u) which gave a quenching factor around 2.56. We hypothesized a scheme for the quenching of self-trapped exciton states (Figure 3.19). This scheme results in charge transfer from the conduction band of calcium titanate to Ag NPs.

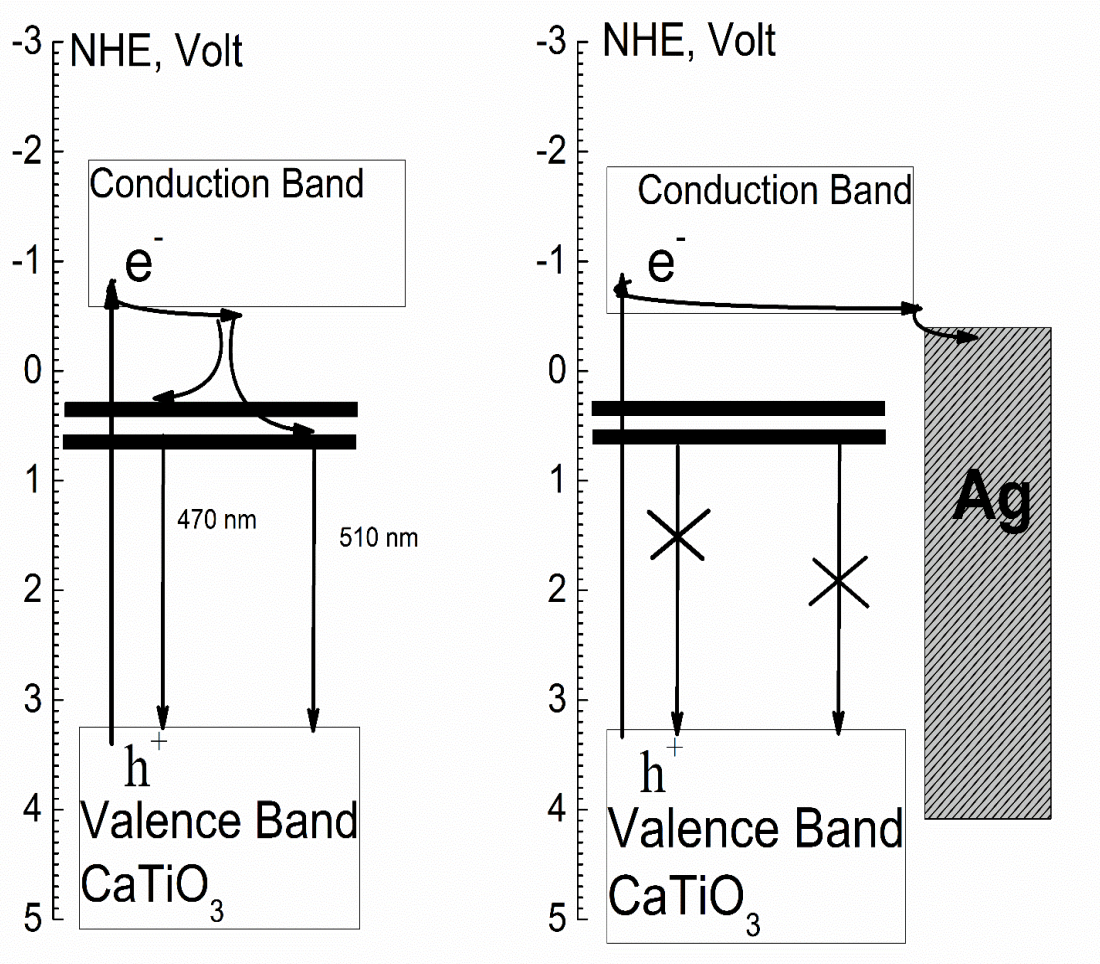

Figure 3.19. The quenching scheme of self-trapped excitons in calcium titanate.

3.5. Characterization of mesoporous calcium titanate

3.5.1. The adsorption–desorption isotherm

The adsorption-desorption isotherm of the synthesized mesoporous $CaTiO_3$ photocatalyst was collected at cryo temperature (77K) after the sample was degassed for 8 hours at 200^o C to remove adsorbed water and air. From the adsorption–desorption isotherm results, the sol-gel synthesized meso$CaTiO_3$ calcined at 600^o C shows a type IV IUPAC pattern (Figure 3.20) with a distinct hysteresis loop [13], which is the main characteristic of mesoporous materials. A sharp increase in adsorption volume of N_2 could be observed at high relative pressure (P/P_0). This sharp increase results from the capillary condensation of N_2 inside the mesopores, indicating the fairly small pore size of the samples because the value of inflection point at a high P/P_0 position directly relates to the pore dimension [10].

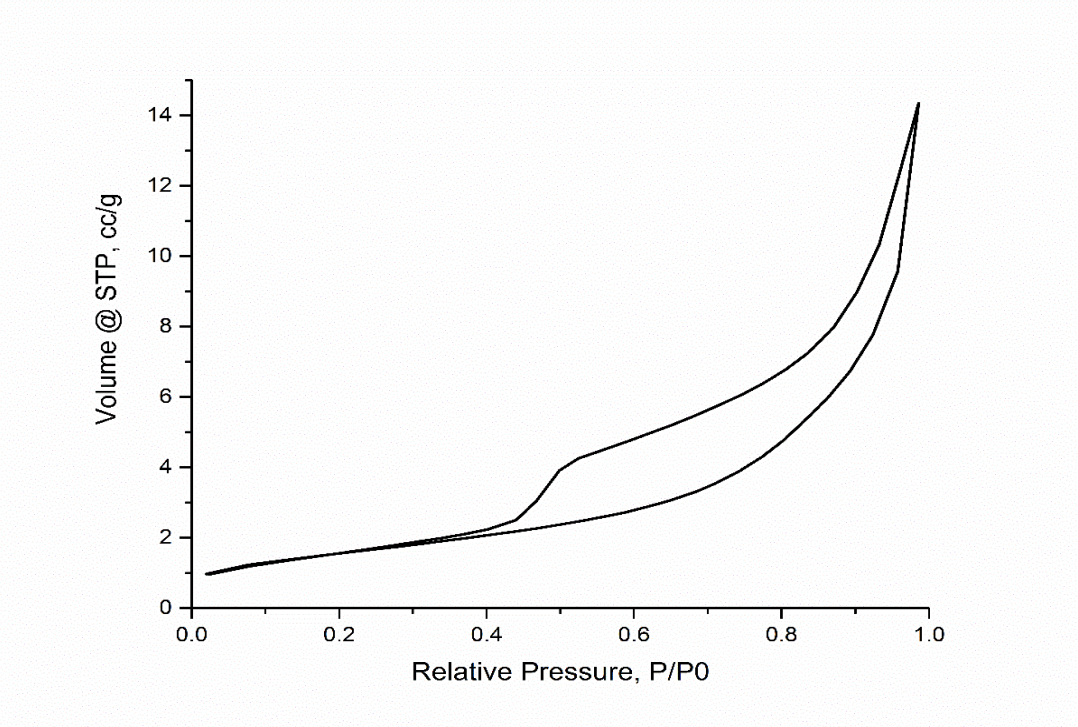

Figure 3.20. Nitrogen adsorption-desorption isotherms at 77 K.

3.5.2. The BET surface area

Some properties such as BET surface area, mean mesopore diameter, and total pore volume are obtained from N_2 adsorption-desorption isotherms [15]. To determine the surface area of the mesoporous calcium titanate, we used the multipoint BET method. In this approach, the BET curve is limited to the adsorption isotherm ranging from $P/P_0 = 0.05$ to 0.35, and at least 5 points are required to obtain the surface area. The adsorption data indicate the BET surface area of our material is 10. 37 m^2g^{-1}.

3.5.3. The determination of pore size

The pore size distribution was calculated by the Barrett- Joynes- Halenda (BJH) method from the desorption branch of the BET curve. The distribution of pore volume with respect to pore size is called a pore size distribution [12]. It is reported that the desorption isotherm is more appropriate than the adsorption isotherm for evaluating the pore size distribution of an adsorbent [10]. The desorption branch of the isotherm, for the same volume of gas, exhibits a lower relative pressure, resulting in a lower free energy state. Thus, the desorption isotherm is closer to the thermodynamic stability [10]. For mesoporous $CaTiO_3$, the distribution is quite narrow, indicating a uniform pore structure with a pore diameter of 2.1 nm, and pore volume of 0.023 cm^3/ g, Figure 3.21.

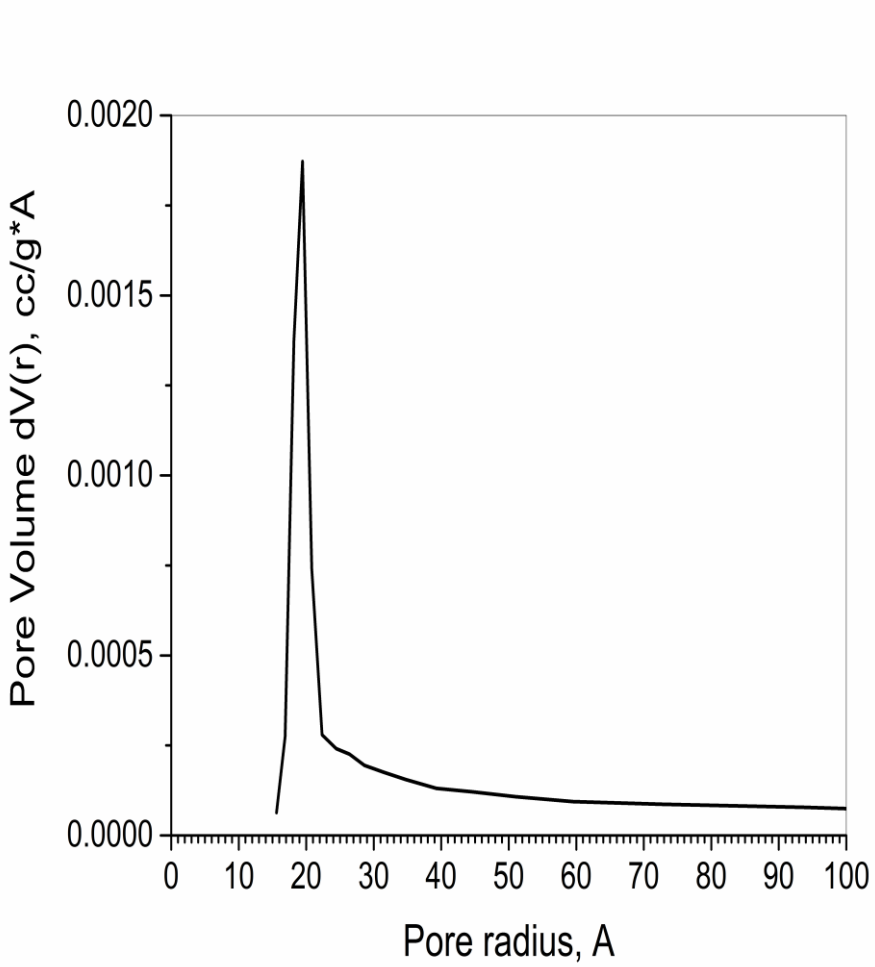

Figure 3.21. BJH pore size distribution calculated from the desorption branch of the isotherm.

3.5.4. UV-vis DRS

Since it was reported by Puangpetch et al. [12] that mesoporous calcium titanate in their work exhibited a cubic lattice structure, we rely on their investigation to determine the band gap of our semiconductor. According to Lee et al. [6] in the first principle study of cubic calcium titanate, $CaTiO_3$ has direct allowed transition and allowed indirect band gaps. We utilized the Tauc plot method in which the reflectance (vertical axis) is plotted as $(F(R).\ E)^{1/n}$, while the absorption wavelengths (horizontal axis) are recalculated to the

energy E (eV), E = 1240/ λ, and n = ½ and n = 2 were used for mesoporous calcium titanate photocatalyst. Then, a line was drawn corresponding to the point of intersection, and the hv value at that point of intersection with the horizontal axis is the band gap energy Eg value, Figure 3.22.

We found that the direct band gap (Figure 3.22, top) of mesoporous $CaTiO_3$ is approximately 3.75 eV (330 nm) while the indirect band gap is around 3.50 eV (Figure 3.22, bottom).

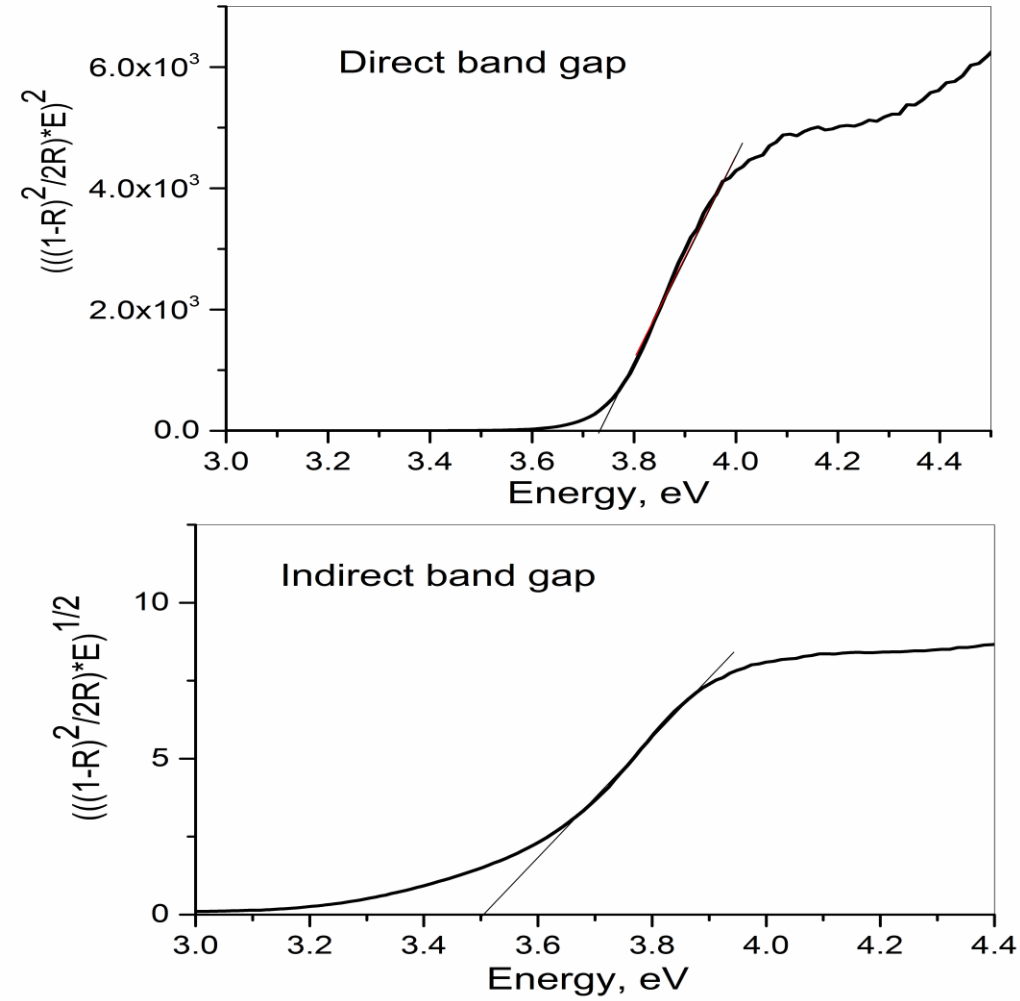

Figure 3.22. The Tauc plot of the direct band gap (top) and indirect band gap (bottom) of mesoporous $CaTiO_3$.

3.6. Photocatalytic activity of hydrogen generation with a silver promoter deposited on mesoporous calcium titanate without an organic donor.

We were interested in using silver (I) fluoride to conduct our photocatalytic reaction to form Ag NPs instead of using $AgNO_3$. It was reported [61] that AgF had better photocatalytic activity than $AgNO_3$ when it was loaded on TiO_2. Ag nanoparticles (NPs) obtained from AgF exhibit also small size [62] which may enhance the efficiency of photocatalytic activity if it is used with the mesoporous catalyst.

Since the photocatalytic activity relies on the properties of the semiconductor such as surface area, pore size, and crystal structure, we tried to use the mesoporous calcium titanate. It is known that increasing the surface area results in a better photocatalytic activity because it affords more active sites. In these experiments, we started our photocatalytic hydrogen production experiments by testing mesoporous calcium titanate (0.055 g) in 15 ml water without any metal promoter by exposing the photocatalytic reactor to a full spectrum of the Hg lamp.

After that, we investigated the ability of mesoporous calcium titanate loaded with Ag NPs without donor to generate hydrogen under UV light irradiation ($\lambda \geq 210$ nm). We attempted to test varying concentrations of AgF, 0.5×10^{-3} M, 1×10^{-3} M, and 5×10^{-3} M, and each sample was illuminated for 20 min before the collection of hydrogen gas. Each concentration exhibited different results; 8 μmol/g.h and 36 μmol/g.h for 0.5×10^{-3} and 1×10^{-3} M, respectively. However, no hydrogen was detected for the concentration 5×10^{-3} M. We assume this is because it is a concentration that leads to covering of the surface of the semiconductor with photo-deposited metal. Figure 3.23 shows the hydrogen production

rate obtained with the hydrogen sensor with the Ag^{+} precursor photo-reduced and deposited to the semiconductor at a concentration 10^{-3} M.

The metal enhanced the photocatalytic activity of mesoporous $CaTiO_3$ to produce hydrogen even without a donor due to the decrease of the recombination between holes and electrons.

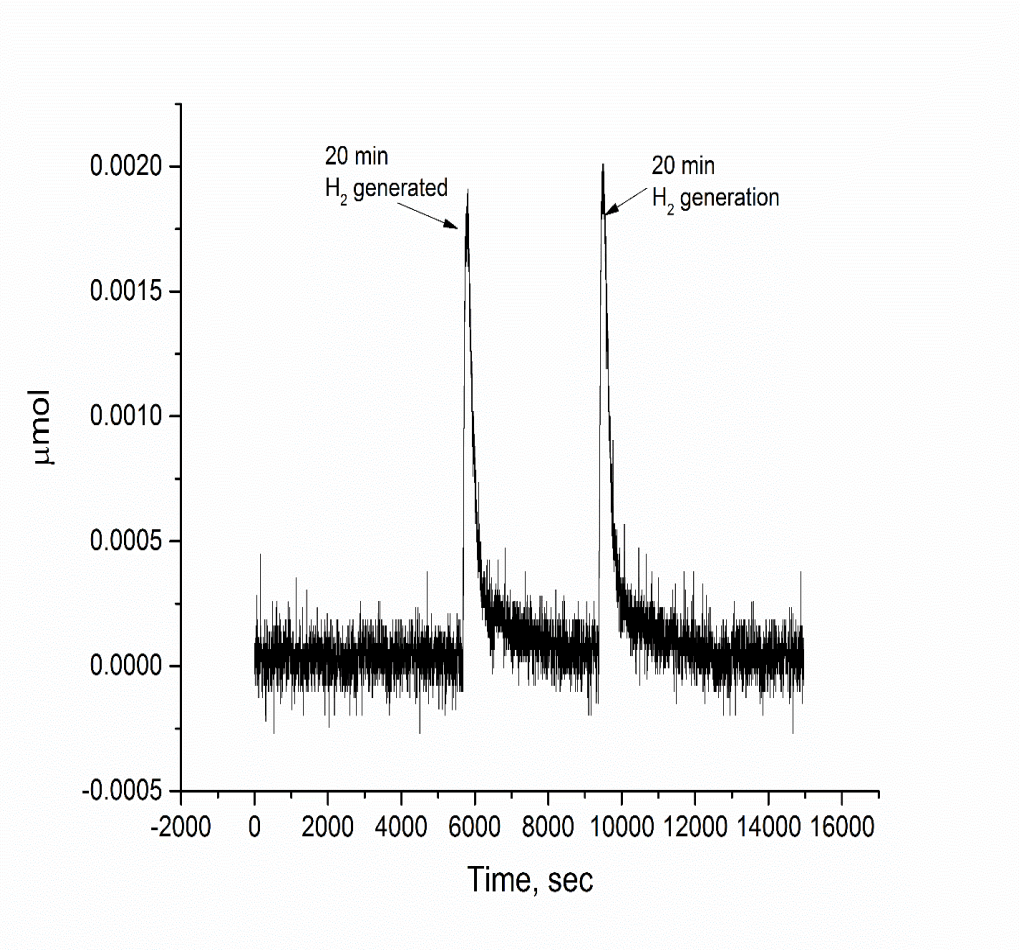

Figure 3.23. Hydrogen production rate, µmol with Ag/mesoporous $CaTiO_3$.

We decided to check the stability of silver loaded on mesoporous calcium titanate by illuminating the photocatalytic reaction for 6 hours: the volume of water was increased to 350 ml using a quartz flask (500 ml) and the amount of catalyst was 1 g. The content of Ag in the catalyst was optimized at $[Ag^{+}] = 10^{-3}$ M to improve the evolution rate of the

hydrogen gas. The evolution rate of H_2 obtained by GC-TCD seemed to increase gradually to reach the maximum in 3 hours and then became stable. We integrated the area of hydrogen peaks every one hour of illumination.

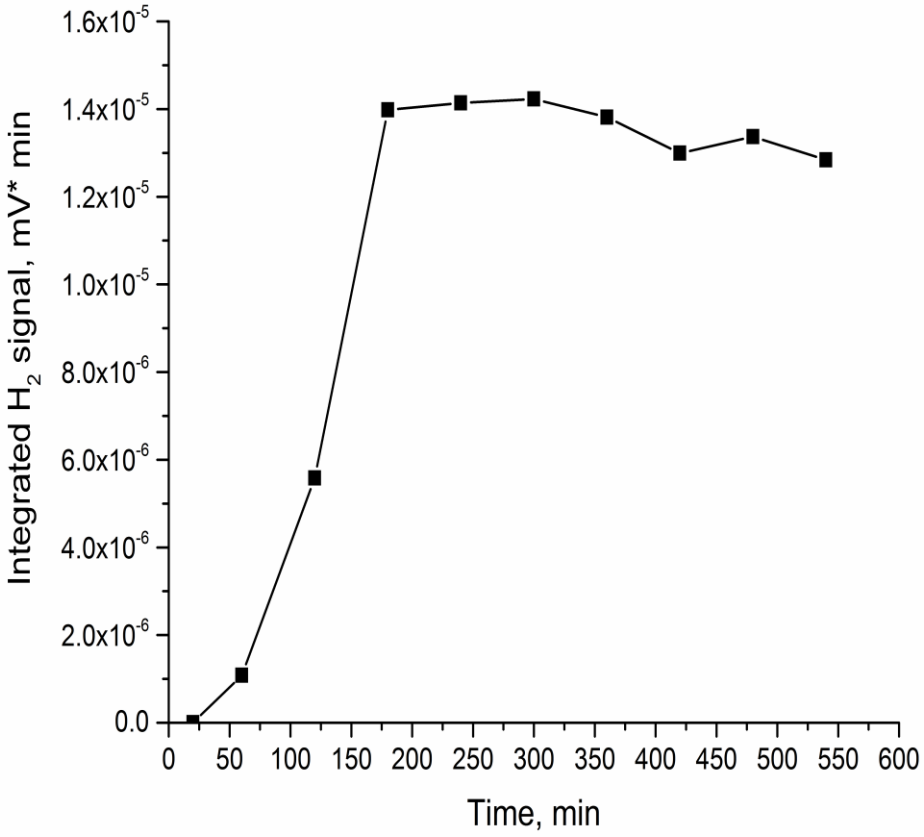

Figure 3.24. Integrated area of hydrogen signal at mV* min.

3.7.1. Comparison of capabilities of conventional and synchronous PL spectroscopy

The PL spectra of mesoporous calcium titanate reveal two mid gap states in the visible region, and it is of interest to compare the capabilities of "conventional" PL emission spectroscopy and synchronous PL spectroscopy at 25º C in resolving these two spectral peaks. Figure 3.25 shows the "conventional" PL emission spectrum of $CaTiO_3$ at λexc = 420 nm, Figure 3.25 A, versus the synchronous PL spectrum of mesoporous $CaTiO_3$ obtained with $\Delta\lambda$ = 60 nm, Figure 3.25 B, plotted in the photon energy domain. Plotting and numeric fitting of the spectra in the photon energy domain rather in the wavelength domain is preferred to determine the energies of these radiative transitions and the full widths at the half maxima, the FWHMs. Both PL spectra in Figure 3.25 have been fitted with the multi-Gaussian function, and an adjusted fitting parameter R^2 = 0.99 indicates a good quality of fitting.

The maximum signal intensity of synchronous PL spectrum in Figure 3.25 B (at ca. 1.8 x 10^6 a.u.) is higher than the signal intensity of conventional (Figure 3.25 A) PL spectrum (at ca. 1.4 x 10^6 a.u. at the peak maximum). The synchronous PL spectrum is narrower which is consistent with the well-known spectral narrowing in the synchronous luminescence spectra of organic compounds compared to the conventional PL emission spectra [41]. In addition, in Figure 3.25 A, the excitation (the Rayleigh) line appears at 2.9 eV (410 nm) which prevents a reliable curve fitting in the high-energy part of the "conventional" PL spectrum. On the other hand, this "Rayleigh artifact" is not present in the synchronous PL spectrum in Figure 3.25 B which helps in the curve fitting.

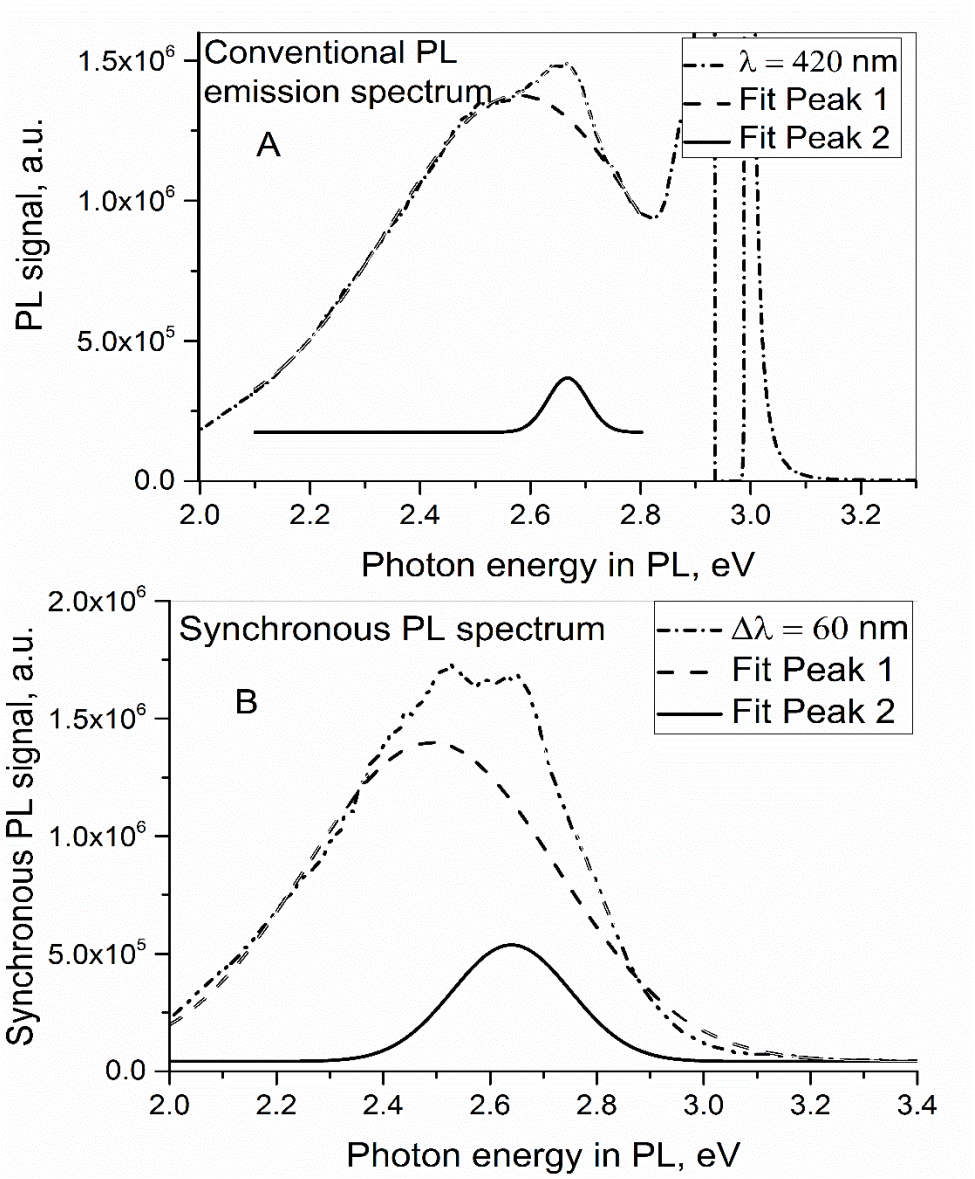

Figure 3.25. A) The conventional PL and B) the synchronous PL of meso calcium titanate.

For the conventional PL spectrum (Figure 3.25 A), the fitted peaks have the following parameters: 1) the peak at 2.57 eV ("green light") with the FWHM = 0.56 eV, 2) the peak at 2.66 eV ("blue light") with the FWHM = 0.08 eV. For the synchronous PL spectrum

(Figure 3.25 B), the fitted peaks have the following parameters: 1) the peak at 2.49 eV ("green light") with a FWHM = 0.54 eV, and 2) the peak at 2.64 eV ("blue light") with a FWHM = 0.25 eV. Thus, in both spectra of Figure 3.25, the two peaks corresponding to "blue light" and "green light" are identified, consistent with the energy diagram in Figure 3.26.

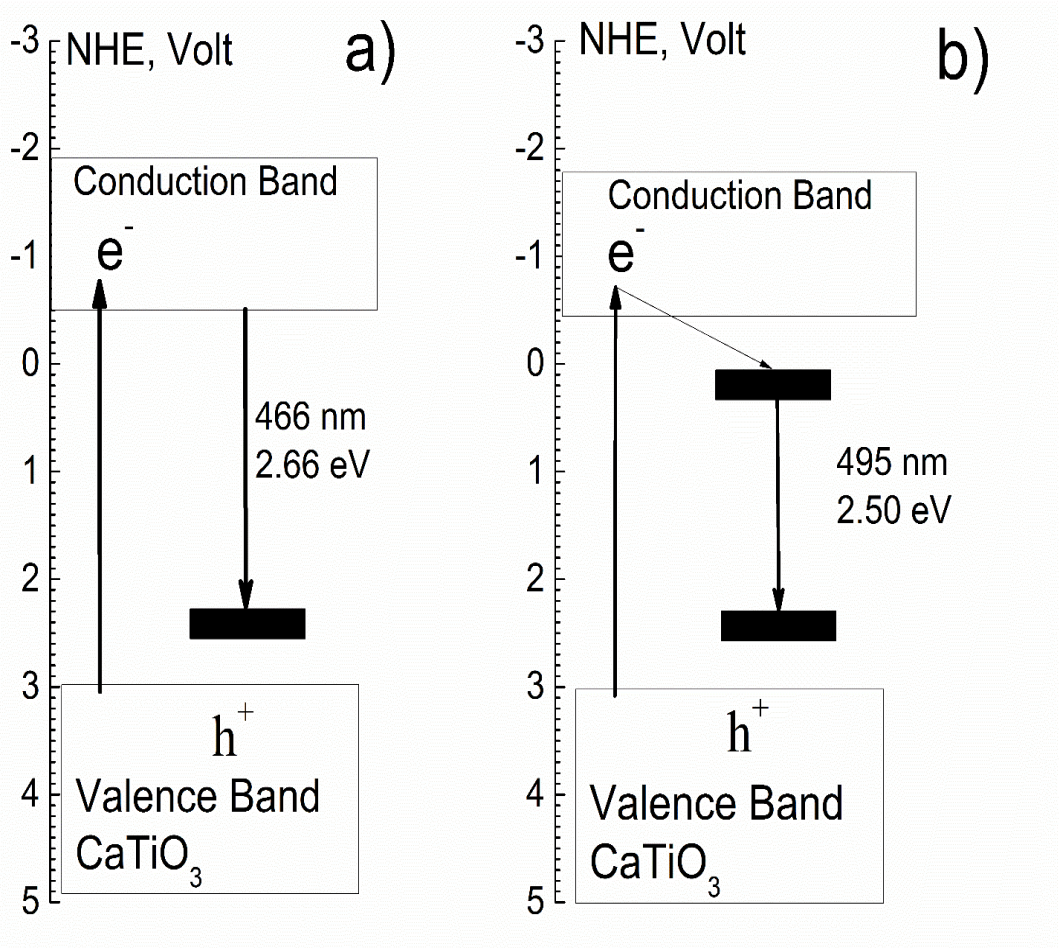

Figure 3.26. The transitions via midgap states in mesoporous $CaTiO_3$.

The FWHMs of the PL peaks are expected to correlate with their origin. The PL peak of "blue light" originating in the transition from the CBM to the low-energy midgap multiplet of states is assumed to have different FWHM from that of the "green light"

originating in the transition from the high energy multiplet to the low-energy multiplet of midgap states. This model is consistent with the FWHMs of the peaks due to "blue emission" (2.64 eV) and "green emission" (2.49 eV) in synchronous PL spectrum in Figure 3.25 B. The FWHM = 0.55 eV of the "green emission" (2.49 eV) and the FWHM = 0.22 eV of the "blue emission" (2.64 eV) yield the ratio FWHM ("green emission") / FWHM ("blue emission") = 0.55 eV/0.22 eV = 2.5. Assuming the same width, in the energy domain, for the high-energy and low-energy states in Figure 3.26, the ratio FWHM ("green emission") / FWHM ("blue emission") is expected to be equal to 2. However, the high-energy and the low-energy multiplets of states are due to the different kind of states. Therefore, their widths are not the same which explains the FWHM ("green emission") / FWHM ("blue emission") = 0.55 eV/0.22 eV = 2.5.

On the other hand, for "conventional" PL spectrum in Figure 3.25 A, the ratio FWHM ("green emission") / FWHM ("blue emission") = 0.55 eV / 0.08 eV = 6.8. Such a high ratio is much further from the predicted ratio = 2 than the ratio = 2.5 observed in the synchronous PL spectra. Therefore, the spectral FWHMs in the "conventional" PL emission spectrum (Figure 3.25 A) of mesoporous $CaTiO_3$ does not appear to be a good indicator of the origin of radiative transitions in the specific initial and the final states. Therefore, the spectral FWHMs in synchronous PL spectrum (Figure 3.25 B) may be a better indicator of the origin of radiative initial and final states in mesoporous $CaTiO_3$ corresponding to "blue emission" and "green emission" bands.

3.7.2. Determination the origin of radiative transitions from the midgap states in mesoporous $CaTiO_3$

In published work for cubic $SrTiO_3$ [63], the high energy midgap state and the low energy midgap state in $SrTiO_3$ were speculated to be located inside the nanocrystals. It is interesting to determine by experiment the location of these states in mesoporous $CaTiO_3$ using PL spectroscopy and the surface probe molecule.

The water molecule which has high energy of its stretching vibration at ca. 3500 cm^{-1} has been extensively studied as a "probe molecule" in the PL quenching experiments. The luminescence of CdS nanoparticles in reversed micelles was quite intense, but it was quenched by adding small amounts of water [64]. The PL quenching was reversible: evaporation of the solvent and water and reconstituting the dry micellar solution with isooctane resulted in a total recovery of luminescence [64]. The origin of luminescence quenching by water was not reported, but it was thought to be due to the surface phenomena of adsorption of water [64]. Nanoparticles of PbS in inverse micelles showed very weak luminescence, which was significantly increased upon removal of water [65]. Adsorption of water on the nanocrystalline calcium titanate was recently studied [66] and concluded to be a surface process. We decided to determine if "green emission" or "blue emission" from our mesoporous $CaTiO_3$ were due to the surface states. We conducted the PL experiments with the removal of adsorbed water by heating and the following adsorption of water onto $CaTiO_3$.

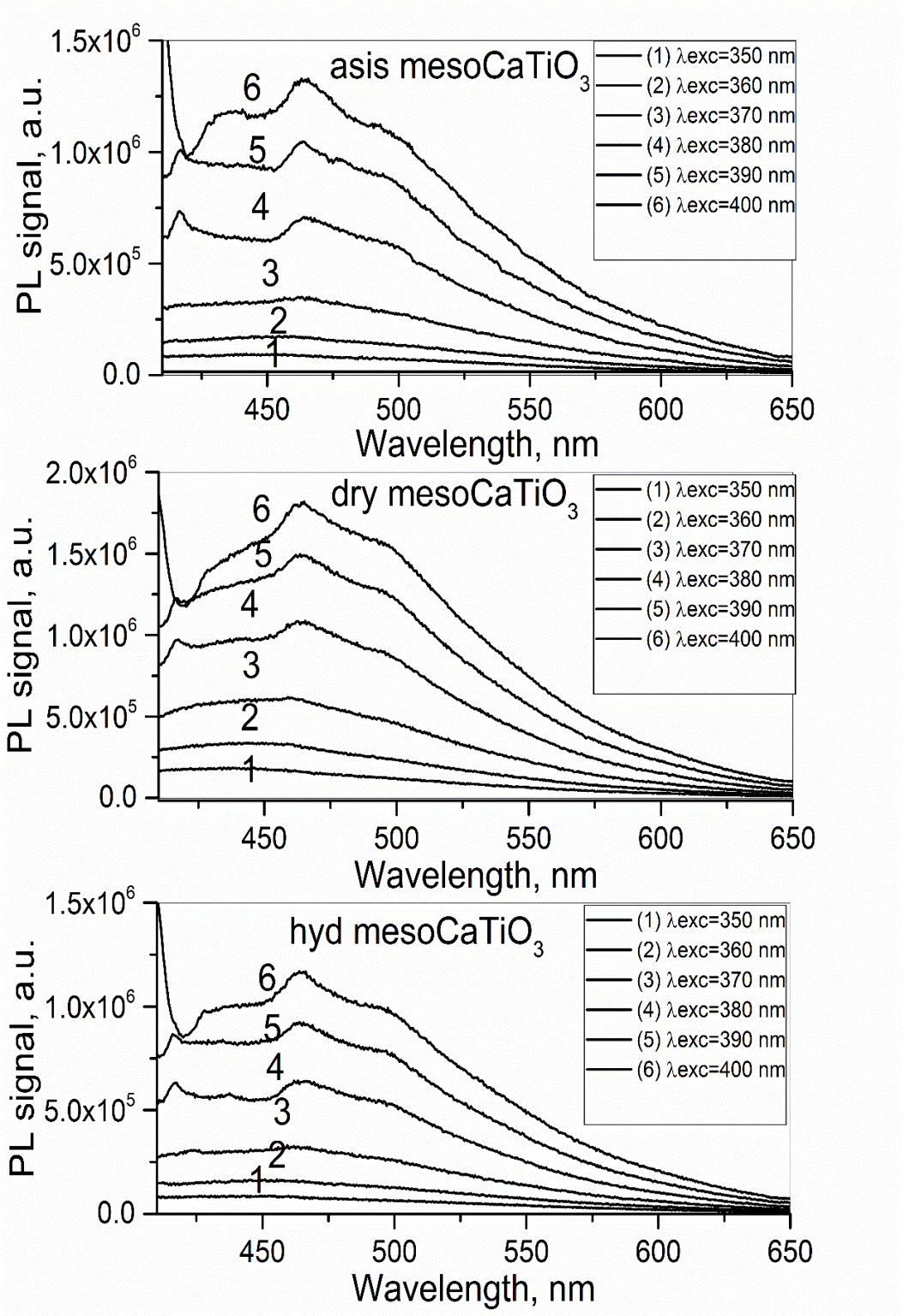

Figure 3.27. The PL spectra of $CaTiO_3$. The as$CaTiO_3$ (top), before drying. The dr$CaTiO_3$ (middle), after drying. The hyd$CaTiO_3$, after hydration (bottom).

Figure 3.27 (top) shows the excitation wavelength-dependent PL emission spectra of mesoporous $CaTiO_3$ before drying. The λexc was varied between the one corresponding to the excitation at the indirect bandgap (λexc = 350 nm) towards λexc = 400 nm. Figure 3.27 (middle) shows the PL spectra after drying. It can be seen that upon drying, there was an increase of the PL signal, by a factor ~1.5, (compare Figure 3.27 (top) and Figure 3.27 (middle)).

Figure 3.27 (bottom) shows the PL spectra after the subsequent hydration in water vapors at room temperature. Upon hydration of $CaTiO_3$, there was a significant decrease of the PL signal, by a factor ~ 1.5, (compare Figure 3.27 (bottom) and Figure 3.27 (middle)). Table 4 shows the change of mass of $CaTiO_3$ after drying and the following humidification, as well as the resultant changes in the intensity of the PL integrated signal. For a quantitative analysis of the efficiency of PL quenching by adsorbed water, an excitation with specific photon energies was conducted, namely with at λexc = 350 nm and λexc = 400 nm. At the λexc = 350 nm, both "blue emission" and ca. 460 nm and "green emission" at ca. 495 nm are observed as one broad spectrum, and at λexc = 400 nm, a "blue emission" at ca. 466 nm is a spectral maximum. An integration of the PL spectrum collected at λexc = 350 nm was conducted in the range λem = 380 - 650 nm; for λexc = 400 nm the integration range was λem = 420 – 650 nm.

Table 4. Change of mass of mesoporous $CaTiO_3$ after drying and hydration, and the change in intensity of the PL at the extra-bandgap and the indirect bandgap excitation.

Material	**Mass, g**	**Change in mass, g**	**Integrated PL signal at λexc = 350 nm, a.u.**	**Integrated PL signal at λexc = 400 nm, a.u.**
asis$CaTiO_3$	0.3425	-	1.36×10^7	1.60×10^8
dr$CaTiO_3$	0.3346	-0.0079	2.65×10^7	2.15×10^8
hyd$CaTiO_3$	0.3437	+0.0091	1.31×10^7	1.40×10^8
dr$CaTiO_3$	0.3328	-0.0109	2.52×10^7	2.05×10^8
hyd$CaTiO_3$ for 2 days	0.3491	+0.0163	1.32×10^7	1.37×10^8

In the hydration step leading to hyd$CaTiO_3$, slightly more water was adsorbed than was desorbed in the drying step of (partially hydrated) asis$CaTiO_3$, Table 4. Consequently, the integrated PL signal at λexc = 350 nm for the hyd$CaTiO_3$ at 1.31×10^7 a.u. was lower than that for asis$CaTiO_3$ at 1.36×10^7 a.u., apparently indicating that the higher amount of adsorbed water caused the lower intensity of the PL signal. The same trend is also observed for the PL data with λexc = 400 nm (Table 4). For both λexc = 350 nm and λexc = 400 nm, the integrated PL signal increased by a factor ~ 1.5 upon the removal of adsorbed water, and the integrated PL signal has subsequently decreased by about the same factor upon adsorption of water vapor.

Therefore, the reversible de-quenching and quenching of the PL from the mesoporous $CaTiO_3$ by desorption/adsorption of water vapor (Figure 3.27 and Table 4) onto the surface [66] of $CaTiO_3$ suggests that the initial and final sates for the radiative transitions observed in the PL spectra are associated with the surface states. Namely, quenching of the PL due to both "blue emission" and "green emission" upon adsorption of water allows a conclusion that both multiplets of the midgap states in Figure 3.26 are the surface states.

3.8. The in-situ kinetics of the PL quenching of Ag/ mesoporous $CaTiO_3$ composite

Having detected the PL emission bands from the composite of mesoporous calcium titanate with Ag NPs, we proceeded to study the kinetics of the quenching of this composite using time-dependent in-situ photoluminescence spectroscopy. We set the sample temperature at 25^o C and the excitation wavelength at 380 nm, which is sub-band excitation of the mesoporous $CaTiO_3$ catalyst, with continuous stirring of the suspension. Figure 3.28 shows the in-situ PL emission spectra of the composite of mesoporous $CaTiO_3$ with AgF in liquid water. Each progressive scan of the spectrum took 1.16 minutes, and the scans are shown in Figure 3.28.

First, we observed that the emission bands at 460 - 495 nm from the composite in Figure 3.28, steadily decreased in intensity as the photoreaction was proceeding. The intensity kept decreasing for about 10 scans (approximately 13 minutes), after that the intensity of these emission bands decreased at a much slower speed than before. After scan # 19 (approximately 20 minutes total photo-deposition time), the photoluminescence spectra did not decrease. Thus, the equilibrium of the photo-reduction process was reached.

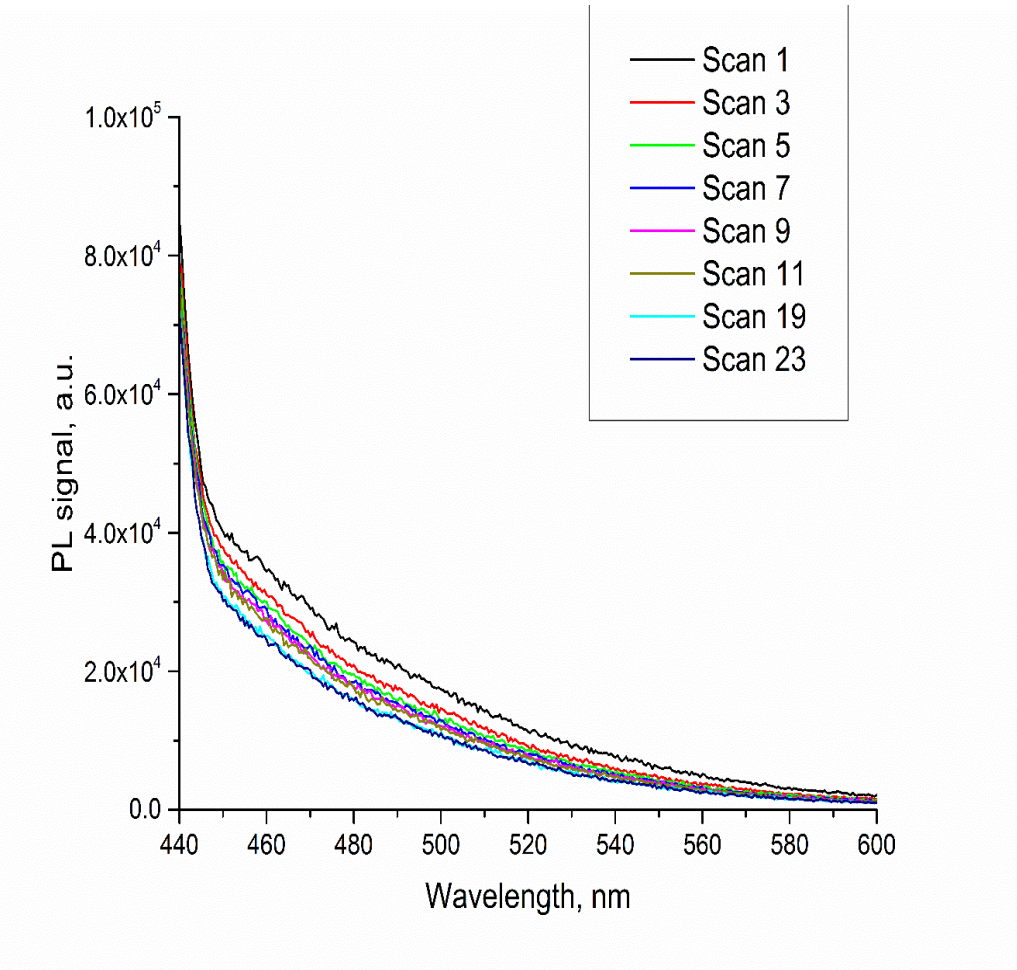

Figure 3.28. The PL spectra of Ag/mesoporous $CaTiO_3$ at λexc = 380 nm.

Next, we attempted to analyze the dependence of the integrated area in the in-situ PL spectra on the photo reaction time at 25 ° C. The dependence of the of the PL quenching corresponds to the integrated kinetic which results in first-order rate law. At the early stage of photo-reduction (before 10 minutes), the integrated area of the photoluminescence spectra was fitted with e^{-kt} function and resulted in a time constant k equal to 3.2 min^{-1}. The coefficient of determination R^2 (correlation coefficient) is 0.994.

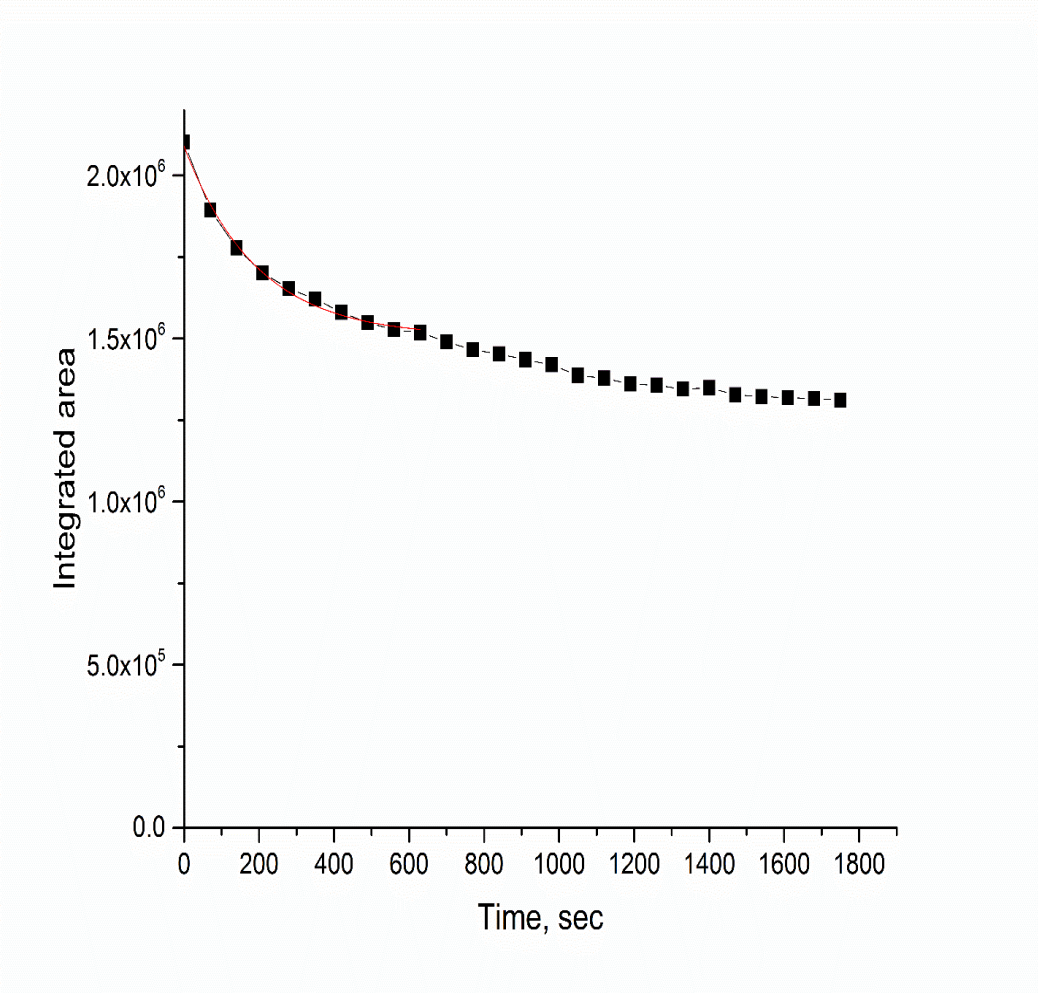

Figure 3.29. The integrated area vs. time of photo-reduction.

4. Summary

We have studied photocatalytic hydrogen production due to silver nanoparticles deposited on calcium titanate with a sacrificial organic donor, glycerol, under UV irradiation. We also have investigated the photocatalytic hydrogen production of Ag NPs deposited on mesoporous $CaTiO_3$ without a sacrificial donor.

In the research with nanocrystalline $CaTiO_3$ loaded with Ag NPs, we conducted the characterization of the $CaTiO_3$ using spectroscopic analysis. For example, we used Raman spectroscopy to identify the crystal structure of the semiconductor which was found to be an orthorhombic. Then, through utilizing UV/Vis diffuse reflectance spectroscopy, we determined the direct band gap of $CaTiO_3$ which helped us later with our study by the photoluminescence spectroscopy. From the PL spectroscopy, we learned about the defects and STEs in $CaTiO_3$ which affect the photocatalytic activity under UV and visible light and charge transfer between the semiconductor and the metal. Further, when we studied the photocatalytic hydrogen production of $CaTiO_3$ and Ag NPs as promotor in the presence of glycerol, we observed that the semiconductor was able to produce hydrogen under UV light with some capability to produce it under the visible light.

In our research with mesoporous $CaTiO_3$ and Ag NPs as promotors without a sacrificial donor, we investigated the ability of the semiconductor and metal to produce hydrogen under UV illumination. We also characterized the two mid gap states within the forbidden gap of the mesoporous $CaTiO_3$ semiconductor using PL emission and synchronous PL spectroscopy. Then, we studied the effect of the hydration on these midgap states by studying their fluorescence. We found that midgap states are surface states because they could be quenched by hydration.

5. Future plans

The rate of hydrogen generation depends on the amounts of composite photocatalyst metal/semiconductor present in the suspension. In the in-situ photochemical synthesis of composite photocatalyst, it takes some time before the final amount of composite metal/semiconductor is formed from the two precursors: semiconductor and metal. Thus, during this in-situ synthesis period, the amount of composite photocatalyst is increasing, and the photocatalytic hydrogen generation rate will also be changed. Therefore, it is important to learn about the time scale of formation of the composite photocatalyst and associated chemical mechanisms, including the kinetics rate laws of formation of composite photocatalysts, but the information is not available. Possible future plans include refining the methodology of the in-situ PL spectroscopy conducted directly in the suspension, and calibration of the PL spectra against the concentration of the active form of the composite photocatalyst to learn about the kinetic mechanism of its formation and associated rate law(s).

The temporal stability of the in-situ prepared composite photocatalyst may change upon its operation due to the changes in the pH, re-dissolution or clustering of deposited metal etc., on the time scale of days or longer. The long-term testing of the stability of the composite photocatalyst by an appropriate in-situ spectroscopy may provide information about mechanisms of long-term stability, and this is important for practical uses of composite photocatalysts.

The accepted mechanism of photocatalytic enhancement with metal-promoted semiconductors is charge separation via the transfer of the photoexcited electron from the CB of the semiconductor to the electronic states in deposited metallic nanoparticles. The

second possible mechanism of the charge-transfer is via the photoexcitation of electronic states in the supported metal via excitation of the surface plasmon resonance (SPR), followed by injection of the photoexcited electron from the metal to the semiconductor. This mechanism is referred to as plasmonic mechanism of charge transfer. The in-situ PL spectroscopy conducted directly in the photocatalytic suspension as developed by us may be capable of revealing plasmonic mechanism of charge transfer in composite photocatalysts.

Based on our observation of emission from the two different kinds of strongly trapped excitons (STEs) in both nanocrystalline and mesoporous $CaTiO_3$, our working hypothesis is that one of them is a bulk STE, while the other one is a surface-localized STE. In the future mechanistic studies, the time-resolved PL spectroscopy (the subnanosecond time) would be useful to learn about the radiative lifetimes of these two different kinds of the STEs in calcium titanate. The controlled adsorption/desorption of water is expected to affect the surface localized STEs, but not the bulk excitons. The time-resolved PL spectroscopy would be a complementary method to the synchronous PL spectroscopy to differentiate between these two kinds of the STE and to assign them.

References

1. Liu, J.; Sun, Y.; Li, Z.; Li, S.; Zhao, J., Photocatalytic hydrogen production from water/methanol solutions over highly ordered Ag–$SrTiO_3$ nanotube arrays. International Journal of Hydrogen Energy 2011, 36 (10), 5811-5816.

2. Castellote, M.; Bengtsson, N., Principles of TiO_2 photocatalysis. In Applications of Titanium Dioxide Photocatalysis to Construction Materials, Springer: 2011; pp 5-10.

3. Zhang, H.; Chen, G.; Li, Y.; Teng, Y., Electronic structure and photocatalytic properties of copper-doped $CaTiO_3$. International Journal of Hydrogen Energy 2010, 35 (7), 2713-2716.

4. Kanhere, P.; Chen, Z., A review on visible light active perovskite-based photocatalysts. Molecules 2014, 19 (12), 19995-20022.

5. Zieliñska, B.; Borowiak-Palen, E.; Kalenczuk, R. J., Photocatalytic hydrogen generation over alkaline-earth titanates in the presence of electron donors. International Journal of Hydrogen Energy 2008, 33 (7), 1797-1802.

6. Lee, H.; Mizoguchi, T.; Yamamoto, T.; Ikuhara, Y., First principles study on intrinsic vacancies in cubic and orthorhombic $CaTiO_3$. Materials Transactions 2009, 50 (5), 977-983.

7. Yashima, M.; Ali, R., Structural phase transition and octahedral tilting in the calcium titanate perovskite $CaTiO_3$. Solid State Ionics 2009, 180 (2), 120-126.

8. Gu, Y.; Rabe, K.; Bousquet, E.; Gopalan, V.; Chen, L.-Q., Phenomenological thermodynamic potential for $CaTiO_3$ single crystals. Physical Review B 2012, 85 (6), 064117.

9. Boudali, A.; Abada, A.; Khodja, M. D.; Amrani, B.; Amara, K.; Khodja, F. D.; Elias, A., Calculation of structural, elastic, electronic, and thermal properties of orthorhombic $CaTiO_3$. Physica B: Condensed Matter 2010, 405 (18), 3879-3884.

10. Machado, A. E.; Borges, K. A.; Silva, T. A.; Santos, L. M.; Borges, M. F.; Machado, W. A.; Caixeta, B. P.; Oliveira, S. M.; Trovó, A. G.; Patrocínio, A. O., Applications of mesoporous ordered semiconductor materials—Case study of TiO_2. Solar Radiation Applications 2015, pp.87 - 118.

11. McNaught, A. D.; McNaught, A. D., Compendium of chemical terminology. Blackwell Science Oxford: 1997; Vol. 1669.

12. Li, D.; Zhou, H.; Honma, I., Design and synthesis of self-ordered mesoporous nanocomposite through controlled in-situ crystallization. Nature Materials 2004, 3 (1), 65-72.

13. Puangpetch, T.; Sommakettarin, P.; Chavadej, S.; Sreethawong, T., Hydrogen production from water splitting over Eosin Y-sensitized mesoporous-assembled perovskite titanate nanocrystal photocatalysts under visible light irradiation. International Journal of Hydrogen Energy 2010, 35 (22), 12428-12442.

14. Puangpetch, T.; Sreethawong, T.; Yoshikawa, S.; Chavadej, S., Synthesis and photocatalytic activity in methyl orange degradation of mesoporous-assembled $SrTiO_3$ nanocrystals prepared by sol–gel method with the aid of structure-directing surfactant. Journal of Molecular Catalysis A: Chemical 2008, 287 (1), 70-79.

15. Sing, K., The use of nitrogen adsorption for the characterisation of porous materials. Colloids and Surfaces A: physicochemical and Engineering Aspects 2001, 187, 3-9.

16. Anpo, M.; Che, M., Applications of photoluminescence techniques to the characterization of solid surfaces in relation to adsorption, catalysis, and photocatalysis. Advances in Catalysis 1999, 44, 119-257.

17. Zheng, H.; Reaney, I.; De Györgyfalva, G. C.; Ubic, R.; Yarwood, J.; Seabra, M.; Ferreira, V., Raman spectroscopy of $CaTiO_3$-based perovskite solid solutions. Journal of Materials Research 2004, 19 (02), 488-495.

18. McMillan, P.; Ross, N., The Raman spectra of several orthorhombic calcium oxide perovskites. Physics and Chemistry of Minerals 1988, 16 (1), 21-28.

19. Balachandran, U. t.; Eror, N., Laser-induced Raman scattering in calcium titanate. Solid State Communications 1982, 44 (6), 815-818.

20. Stone, F. S., UV-visible diffuse reflectance spectroscopy applied to bulk and surface properties of oxides and related solids. In Surface Properties and Catalysis by Non-metals, Springer: 1983; pp 237-272.

21. López, R.; Gómez, R., Band-gap energy estimation from diffuse reflectance measurements on sol–gel and commercial TiO_2: a comparative study. Journal of Sol-gel Science and Technology 2012, 61 (1), 1-7.

22. Murphy, A., Band-gap determination from diffuse reflectance measurements of semiconductor films, and application to photoelectrochemical water-splitting. Solar Energy Materials and Solar Cells 2007, 91 (14), 1326-1337.

23. Rafferty, B.; Brown, L., Direct and indirect transitions in the region of the band gap using electron-energy-loss spectroscopy. Physical Review B 1998, 58 (16), 10326.

24. Lin, H.; Huang, C.; Li, W.; Ni, C.; Shah, S. I.; Tseng, Y.-H., Size dependency of nanocrystalline TiO_2 on its optical property and photocatalytic reactivity exemplified by 2-chlorophenol. Applied Catalysis B: Environmental 2006, 68 (1), 1-11.

25. Wold, A., Photocatalytic properties of titanium dioxide (TiO_2). Chemistry of Materials 1993, 5 (3), 280-283.

26. Xu, Y.; Schoonen, M. A., The absolute energy positions of conduction and valence bands of selected semiconducting minerals. American Mineralogist 2000, 85 (4), 543-556.

27. Yu, J.; Hai, Y.; Jaroniec, M., Photocatalytic hydrogen production over CuO-modified titania. Journal of Colloid and Interface Science 2011, 357 (1), 223-228.

28. Pal, U.; Ghosh, S.; Chatterjee, D., Effect of sacrificial electron donors on hydrogen generation over visible light–irradiated nonmetal-doped TiO_2 photocatalysts. Transition Metal Chemistry 2012, 37 (1), 93-96.

29. Jang, J.; Borse, P.; Lee, J.; Lim, K.; Jung, O.; Jeong, E.; Bae, J.; Kim, H., Photocatalytic hydrogen production in water-methanol mixture over iron-doped $CaTiO_3$. Bull. Korean Chemical Society 2011, 32 (1), 95-99.

30. Nishimoto, S.; Matsuda, M.; Miyake, M., Photocatalytic activities of Rh-doped $CaTiO_3$ under visible light irradiation. Chemistry Letters 2006, 35 (3), 308-309.

31. Liu, S.; Qu, Y.; Li, R.; Wang, G.; Li, Y., Photocatalytic activity of $MTiO_3$ (M= Ca, Ni, and Zn) nanocrystals for water decomposition to hydrogen. Journal of Materials Research 2014, 29 (11), 1295-1301.

32. Zhang, H.; Chen, G.; He, X.; Xu, J., Electronic structure and photocatalytic properties of Ag–La codoped $CaTiO_3$. Journal of Alloys and Compounds 2012, 516, 91-95.

33. Mizoguchi, H.; Ueda, K.; Orita, M.; Moon, S.-C.; Kajihara, K.; Hirano, M.; Hosono, H., Decomposition of water by a $CaTiO_3$ photocatalyst under UV light irradiation. Materials Research Bulletin 2002, 37 (15), 2401-2406.

34. Chen, Y.; Tian, G.; Ren, Z.; Pan, K.; Shi, Y.; Wang, J.; Fu, H., Hierarchical core–shell carbon nanofiber@ $ZnIn_2S_4$ composites for enhanced hydrogen evolution performance. ACS Applied Materials & Interfaces 2014, 6 (16), 13841-13849.

35. Bowker, M.; Davies, P. R.; Al-Mazroai, L. S., Photocatalytic reforming of glycerol over gold and palladium as an alternative fuel source. Catalysis Letters 2009, 128 (3-4), 253-255.

36. Chen, X.; Zheng, Z.; Ke, X.; Jaatinen, E.; Xie, T.; Wang, D.; Guo, C.; Zhao, J.; Zhu, H., Supported silver nanoparticles as photocatalysts under ultraviolet and visible light irradiation. Green Chemistry 2010, 12 (3), 414-419.

37. Yeshchenko, O. A.; Dmitruk, I. M.; Alexeenko, A. A.; Losytskyy, M. Y.; Kotko, A. V.; Pinchuk, A. O., Size-dependent surface-plasmon-enhanced photoluminescence from silver nanoparticles embedded in silica. Physical Review B 2009, 79 (23), 235438.

38. Smitha, S.; Nissamudeen, K.; Philip, D.; Gopchandran, K., Studies on surface plasmon resonance and photoluminescence of silver nanoparticles. Spectrochimica Acta Part A: Molecular and Biomolecular Spectroscopy 2008, 71 (1), 186-190.

39. Gilliland, G., Photoluminescence spectroscopy of crystalline semiconductors. Materials Science and Engineering: R: Reports 1997, 18 (3), 99-399.

40. Patra, D.; Ghaddar, T. H., Application of synchronous fluorescence scan spectroscopy for size dependent simultaneous analysis of CdTe nanocrystals and their mixtures. Talanta 2009, 77 (4), 1549-1554.

41. Dinh, T. V., Multicomponent analysis by synchronous luminescence spectrometry. Analytical Chemistry 1978, 50 (3), 396-401.

42. Kernazhitsky, L.; Shymanovska, V.; Gavrilko, T.; Naumov, V.; Fedorenko, L.; Kshnyakin, V.; Baran, J., Room temperature photoluminescence of anatase and rutile TiO_2 powders. Journal of Luminescence 2014, 146, 199-204.

43. Moura, F.; Simoes, A.; Deus, R.; Silva, M.; Varela, J. A.; Longo, E., Intense photoluminescence emission at room temperature in calcium copper titanate powders. Ceramics International 2013, 39 (4), 3499-3506.

44. Zhang, W.; Yin, Z.; Zhang, M., Study of photoluminescence and electronic states in nanophase strontium titanate. Applied Physics A 2000, 70 (1), 93-96.

45. Abazovic, N. D.; Cˇomor, M. I.; Dramicanin, M. D.; Jovanovic, D. J.; Ahrenkiel, S. P.; Nedeljkovic, J. M., Photoluminescence of anatase and rutile TiO_2 particles. The Journal of Physical Chemistry B 2006, 110 (50), 25366-25370.

46. Borghs, G.; Bhattacharyya, K.; Deneffe, K.; Van Mieghem, P.; Mertens, R., Band-gap narrowing in highly doped n-and p-type GaAs studied by photoluminescence spectroscopy. Journal of Applied Physics 1989, 66 (9), 4381-4386.

47. Zhang, W.; Yin, Z.; Zhang, M.; Du, Z.; Chen, W., Roles of defects and grain sizes in photoluminescence of nanocrystalline $SrTiO_3$. Journal of physics: Condensed Matter 1999, 11 (29), 5655.

48. Williams, R.; Song, K., The self-trapped exciton. Journal of Physics and Chemistry of Solids 1990, 51 (7), 679-716.

49. Lakowicz, J. R., Quenching of fluorescence. In Principles of Fluorescence Spectroscopy, Springer: 1983; pp 257-301.

50. Dai, J.; McKee, M. L.; Samokhvalov, A., Fluorescence of A100 MOF and adsorption of water, indole, and naphthalene on A100 by the spectroscopic, kinetic, and DFT studies. The Journal of Physical Chemistry C 2015, 119 (5), 2491-2502.

51. Cavalcante, L.; Marques, V.; Sczancoski, J.; Escote, M.; Joya, M.; Varela, J. A.; Santos, M.; Pizani, P.; Longo, E., Synthesis, structural refinement and optical behavior of $CaTiO_3$ powders: a comparative study of processing in different furnaces. Chemical Engineering Journal 2008, 143 (1), 299-307.

52. Zhang, A.; Zhang, J.; Fang, Y., Photoluminescence from colloidal silver nanoparticles. Journal of Luminescence 2008, 128 (10), 1635-1640.

53. Lu, S.; Xu, Z.; Chen, H.; Mak, C.-l.; Wong, K.-h.; Li, K.; Cheah, K., Time-resolved photoluminescence of barium titanate ultrafine powders. Journal of Applied Physics 2006, 99 (6), 1-4.

54. Boutinaud, P.; Pinel, E.; Dubois, M.; Vink, A.; Mahiou, R., UV-to-red relaxation pathways in $CaTiO_3$: Pr^{3+}. Journal of Luminescence 2005, 111 (1), 69-80.

55. Grabner, L.; Stokowski, S., Photoluminescence of Cr-doped $CaTiO_3$. Physical Review B 1970, 2 (11), 4351.

56. Patel, K.; Kapoor, S.; Dave, D.; Mukherjee, T., Synthesis of nanosized silver colloids by microwave dielectric heating. Journal of Chemical Sciences 2005, 117 (1), 53-60.

57. Kisch, H., On the problem of comparing rates or apparent quantum yields in heterogeneous photocatalysis. Angewandte Chemie 2010, 122 (50), 9782-9783.

58. Korzhak, A. V.; Ermokhina, N. I.; Stroyuk, A. L.; Bukhtiyarov, V. K.; Raevskaya, A. E.; Litvin, V. I.; Kuchmiy, S. Y.; Ilyin, V. G.; Manorik, P. A., Photocatalytic hydrogen evolution over mesoporous TiO_2/metal nanocomposites. Journal of Photochemistry and Photobiology A: Chemistry 2008, 198 (2), 126-134.

59. Wu, F.; Hu, X.; Fan, J.; Liu, E.; Sun, T.; Kang, L.; Hou, W.; Zhu, C.; Liu, H., Photocatalytic activity of Ag/TiO_2 nanotube arrays enhanced by surface plasmon resonance and application in hydrogen evolution by water splitting. Plasmonics 2013, 8 (2), 501-508.

60. Watanabe, M.; Hayashi, T.; Yagasaki, H.; Sasaki, S., Luminescence process in anatase TiO_2 studied by time-resolved spectroscopy. International Journal of Modern Physics B 2001, 15 (28), 3997-4000.

61. Lee, W.; Shen, H.; Dwight, K.; Wold, A., Effect of silver on the photocatalytic activity of TiO_2. Journal of Solid State Chemistry 1993, 106 (2), 288-294.

62. Maity, K.; Panda, D. K.; Lochner, E.; Saha, S., Fluoride-induced reduction of Ag (I) cation leading to formation of silver mirrors and luminescent Ag-nanoparticles. Journal of the American Chemical Society 2015, 137 (8), 2812-2815.

63. Kan, D.; Terashima, T.; Kanda, R.; Masuno, A.; Tanaka, K.; Chu, S.; Kan, H.; Ishizumi, A.; Kanemitsu, Y.; Shimakawa, Y.; Takano, M., Blue-light emission at room temperature from Ar^{+}-irradiated $SrTiO_3$. Nature Materials 2005, 4, 816-819.

64. Tata, M.; Banerjee, S.; John, V. T.; Waguespack, Y.; McPherson, G. L., Fluorescence quenching of CdS nanocrystallites in AOT water-in-oil microemulsions. Colloids and Surfaces A: Physicochemical and Engineering Aspects 1997, 127 (1-3), 39-46.

65. Buckner, S. W.; Konold, R. L.; Jelliss, P. A., Luminescence quenching in PbS nanoparticles. Chemical Physics Letters 2004, 394 (4-6), 400-404.

66. Sahu, S. K.; Maram, P. S.; Navrotsky, A., Thermodynamics of nanoscale calcium and strontium titanate perovskites. Journal of the American Ceramic Society 2013, 96 (11), 3670-3676.